Hindawi
Journal of Engineering
Volume 2024, Article ID 9991809, 24 pages
https://doi.org/10.1155/2024/9991809

Research Article

Effects of Heat Transfer Characteristics of R32 and R1234yf with Al_2O_3 Nanoparticle through U-Bend Tube Evaporator

Latifur Islam, Dipayan Mondal, Md. Ashraful Islam, and Palash Das

Department of Mechanical Engineering, Khulna University of Engineering & Technology, Khulna 9203, Bangladesh

Correspondence should be addressed to Dipayan Mondal; dipkuet@me.kuet.ac.bd

Received 31 January 2024; Revised 5 March 2024; Accepted 13 March 2024; Published 27 March 2024

Academic Editor: Angelo Maiorino

This study used the Ansys Fluent® computational fluid dynamics code in conjunction with a volume of fluid multiphase model and phase-change model to analyze the flow boiling evaporation heat transfer coefficient and flow patterns of R32 and R1234yf with Al_2O_3 nanoparticle through the U-bend tube with a curvature ratio for downward-oriented flow. The volume of fluid (VOF) model was used to follow the patterns at the interface, while the SST k-omega model was used to simulate the gas-liquid flow. This work has been validated by utilizing a R134a refrigerant. Simulations were performed at various mass fluxes, vapor qualities, and temperatures to determine the effects of these variables on heat transfer and frictional pressure decrease in the tube. R1234yf shows much better performance than the other pure refrigerants in terms of heat transfer and vaporization. The addition of nanoparticle Al_2O_3 with the refrigerants R32 and R1234yf significantly improved the heat transfer coefficient and increased the vapor fraction. The frictional pressure drop increases with increasing mass flux and decreases with increasing vapor quality due to a significant decrease in the liquid film thickness. The heat transfer coefficient, on the other hand, increases with increasing mass flux and decreases with vapor quality up to a point. There are certain changes in the heat transfer coefficient at the bend. After the bend, the frictional pressure drop increased at a higher rate than before the bend, and the vapor fraction increased at a higher rate.

1. Introduction

Evaporation in U-bend tubes is a highly effective technology that addresses thermal management challenges, as it offers high heat transfer efficiency and lower heat transfer temperature difference. The study of evaporation and heat transfer has attracted a lot of attention in recent years because of its high productivity and wide applications. While designing an evaporator tube, it is essential to consider the heat transfer coefficient, frictional pressure drop, and flow pattern. Nowadays, some popular refrigerants (i.e., R134a, R32, R1234yf, and R410A) are used for the cycle performance in practical refrigeration and air conditioning system appliances. Compared to many other hydrofluorocarbons (HFCs), R32 is an HFC refrigerant with a reduced global warming potential (GWP). Hydrofluoroolefins (HFOs) have lately gained popularity for their low GWP value and other advantageous environmental properties: GWP for R1234yf is 4 [1], R1234ze(E) is 6 [2, 3], R1234ze(E) is 3 [4], R1336mzz(Z) is 2 [5], and R1336mzz(E) is 18 [6], as well as the viscosity and thermal conductivity of R1336mzz(E) are reported by Mondal et al. [7, 8].

Numerous studies have been conducted to improve the methods for computing the transitions in flow patterns in fluid dynamics. Wu et al. [9] studied the impact of flow behavior in a U-bend adiabatic tube using various flow orientations. Hajal et al. [10] developed a flow pattern map for R134a, R123, R402A, R404A, and R50 evaporation in horizontal tubes under diabatic circumstances. Much research has been carried out to enhance the approaches for computing flow pattern transitions in fluid dynamics. Cheng et al. [11] used dynamic vapor fraction measurement to improve on a technique pioneered by Hajal et al. [10]. Greco and Vanoli [12] developed a simple approach for identifying R134a, R22, and R410a flow pattern transitions. Moreover, Grauso et al. [13] developed a flow characteristic for R1234ze(E) in a horizontal tube and compared it to the approach used by Cheng et al. [11]. Yang et al. [14]

investigated the heat flux, mass flux, and saturation pressure affect flow pattern transitions using R1234ze(E) and R170 refrigerants. For the two-phase case, it was discovered that using huge pressure drops as a system drop will reduce system efficiency. Padilla et al. [15] revised a system for estimating pressure decreases in U-bend tubes caused by differences in geometries and circumstances, especially for the refrigerants R12, R134a, and R410A. Kerpel et al. [16] investigated the frictional pressure loss of R134a in U-bend geometry in another investigation. Moreover, Lima and Thome [17] discovered that the frictional pressure loss for R134a in U-bend tubes was double that of straight tubes. The research used mass transfer relaxation time factors to guarantee that the interface temperature stayed near the saturation temperature [18]. The study also included evaporation mass transfer source terms, which aided in the transfer of mass from the liquid phase to the vapor phase. Schepper et al. [19] combined this model with a phase-change model to follow flow regimes in hydrocarbon feedstock flow boiling evaporation. Meanwhile, Abadi et al. [20] observed the condensation flow patterns of R134a at inclined angles using a user-defined function phase-change model and the aforementioned model. Lillo et al. [21] integrated the model with a phase-change model to investigate the effect of tube form (circular, square, and triangular) on condensation flow patterns of R32 in mini-horizontal channels. Lorenzini et al. [22] utilized the model with a phase-change model to evaluate two-phase cooling in microelectronics. In addition, Li [23] combined the model with a phase-change model to investigate acetone condensation. Aprea et al. [24] reported in their experimental research that HFO1234ze could be a replacement for R134a as the former shows 100 times lower GWP and environmental effect. Maiorino et al. [25] addressed in their research that R152a could be a drop-in replacement of R134a as the former shows a coinciding performance in different parameters measured in this research work. Soni et al. [26] investigated a comparative study of conventional VCR systems using R134a, R152a, R600a, and R290 refrigerants. This investigation was performed for the evaporator temperature at −30~10°C, whereas the condenser temperature at 40~45°C was used to estimate the work input to the compressor and refrigerating effect in the evaporator and COP of the system as well.

Furthermore, the nanorefrigerant is one type of nanofluid that has been touted as having unparalleled refrigeration qualities and increasing the heat transfer coefficient in the refrigeration system. A wide range of substances could be used to create nanoparticles that are suspended in ordinary refrigerants [27]. The size range of nanoparticles is approximately 1~100 nm. Nanoparticles are merely distinct cylinders and strands that are smaller than 100 nm. At a fundamental length size of 100 nm, novel features that produce diverse particles from mass material often increase. To enhance the refrigeration effect, only a blend of nanomolecules can be employed as a structured nanorefrigerant. In contrast to conventional refrigerant, the nanorefrigerant will be able to travel more readily [28]. Majgaonkar [29] presented a review paper regarding the use of nanoparticles in refrigeration systems. When the nanoparticles are mixed with refrigerant in the refrigeration cycle, nanoparticles move with the refrigerant. The refrigerant undergoes a phase change in the condenser and evaporator of refrigeration systems. Studies on the properties of migration during the condensation process are equally important, much as studies on boiling. Nanoparticle migration characteristics were investigated in a pool boiling experiment by Peng et al. [30] and Ding et al. [31]. These studies will be helpful in systems that use flooded evaporators for refrigeration. Moreover, there are also several works on nanoparticles used with refrigerants for a refrigeration system. Hernandez et al. [32] presented an analysis of nanofluid-based simulation where the refrigerants R113, R123, and R134a were mixed with Al_2O_3 nanoparticles at 1 vf% and 5 vf% flowing through a horizontal tube with a constant wall temperature to improve the thermal efficiency of the system. Kumar and Elansezhian [33] conducted an experimental study on Al_2O_3-R134a in VCRS which performed with less energy and there is an improvement in COP. Royal et al. [34] also conducted an experimental study on Al_2O_3-R134a, whereas the inclusion of Al_2O_3 nanoparticle with refrigerant indicates the improvement of the system COP, the power consumption is decreased, and the efficiency of the compressor is advanced. Mallikarjuna et al. [27] conducted research on TiO_2, CuO, and Al_2O_3 with R134a and found a better COP and lower evaporative temperature. Bibin et al. [28] performed a review on using Al_2O_3, CuO, and TiO_2 with R134a and indicated that TiO_2 with R134a refrigerant shows the maximum enhancement in coefficient of performance and Al_2O_3-R134a offers a 27% reduction in power usage when compared to traditional fluids. Vamshi et al. [35] reported a review on the utilization of nanoparticles in refrigeration systems in which various heat transfer characteristics of working fluid with Al_2O_3, TiO_2, CuO, and SiO_2 are to be studied. This review presented correlations used to estimate the viscosity, thermal conductivity, heat transfer coefficient, and Nusselt number. The focus of this study is to blend the Al_2O_3 nanoparticle with pure refrigerants, and utilizing nanofluids such as R32-Al_2O_3 and R1234yf-Al_2O_3 in refrigeration systems can improve the evaporator performance by raising the overall heat transfer coefficient of the system. The higher thermal conductivity of the nanofluid is principally responsible for the increased heat transfer coefficient.

From the aforementioned debate, numerous scholars examined the flow patterns, heat transfer, and pressure drop in tubes with various orientations, including adiabatic and diabatic. However, there are several research studies on U-bend tubes, particularly in diabatic conditions, and flow pattern mapping in U-bend tubes [36]. Therefore, this study aims to address this gap by using numerical methods to investigate heat transfer during flow boiling evaporation of R32, R1234yf, R32-Al_2O_3, and R1234yf-Al_2O_3 in U-bend tubes for descending flow orientation, as well as the development of flow patterns before and after a bend in a downward-oriented flow according to vapor fraction and different mass flux. In order to evaluate the performance of evaporators for a variety of mass fluxes and vapor quality,

measurements have been taken of the heat transfer coefficient, the frictional pressure drop, and the temperature effect on heat transfer. This information can be helpful in the refrigeration and air conditioning processes.

2. Methodology

Refrigerators are an indispensable feature of every family in today's environment. A refrigerator is a device that operates on a continuous cycle to keep the temperature of a cold body (refrigerated space) lower than the ambient temperature. The purpose of a refrigerator is to store food and other perishable items at a low temperature to slow down or prevent the growth of harmful bacteria and other microorganisms. The basic vapor compression refrigeration (VCR) system is depicted in Figure 1, where the evaporator is the important component for providing the primary functions of a refrigerator. To achieve the goal, the heat transfer characteristics through the U-bend tube evaporator will be numerically investigated by utilizing R32 and R1234yf with Al_2O_3 nanoparticles.

2.1. Physical Model. Numerous researchers conducted their works [10–13, 17, 36] using R134a passing through the evaporator tube. The U-bend tube is a very popular configuration in heat exchanger design. Although the U-bend tube configurations may vary in various types, all other tubes can be represented as a single U-bend tube [36] and the following patterns in an adiabatic condition in U-bend of various orientations are observed by Lima and Thome [39]. Therefore, the horizontal U-bend tube (length 1 m, bend radius 10 mm, and diameter 8.1 mm) in the downstream, upstream, and bend sections of the heat exchanger tube was simulated by using ANSYS R20. The simulation was conducted under different conditions, including a mass flux from 35 to 160 kg/m^2·s and a vapor fraction of 0.01–0.91. The model assumed a constant and uniform heat flow on the surface area of the tube, ignoring the impact of fins to simplify the heat flow assumption. However, this simplification is useful in understanding heat transfer methods [40].

2.2. Numerical Model. The study utilized ANSYS Fluent software to conduct simulations. The observed flow is characterized by steady-state flow conditions, and the flow field has a three-dimensional nature. The geometry of the U-bend pipe shape will be generated by using the space claim module of ANSYS. Subsequently, the model was then gridded into a discrete volume of tetrahedral elements. The utilization of suitable mesh parameters and methodologies was employed in order to attain a very similar outcome. The numerical calculations on the model mesh were conducted using ANSYS Fluent. The U-shaped tube was filled with a liquid refrigerant known as R134a. The copper pipe was subject to many constraints, such as the prescribed flow rate of both liquid and gas, a specified pressure at the intake, and a designated temperature at the outer surface of the tube. The movement of the pipe was also restricted. In order to fabricate the flow of vapor and liquid in a system, the vapor and liquid phases were identified as the two main parts of the system. The volume percentages of the liquid and vapor phases were subsequently monitored within the computational domain by utilizing the volume of fluid (VOF) model. The VOF model will be employed to track the interface patterns, while the gas-liquid flow will be simulated with the shear stress transport (SST) k-omega model. The discretization technique employed in this study utilized geo-reconstruction to accurately trace the interfaces. In order to maintain system stability, a pressure implicit operator splitting (SIMPLE) approach was employed to effectively couple the variables of pressure and velocity.

The continuity equation is given based on the vapor fraction as follows [36, 41]:

$$\frac{\partial}{\partial t}\left(\alpha_q \rho_q\right) + \nabla.\left(\alpha_q \rho_q \vec{v}\right) = \sum_{p=1}^{n}\left(\dot{m}_{\mathrm{pq}}\right). \tag{1}$$

The momentum balance formula in the VOF model is as follows:

$$\frac{\partial}{\partial t}\left(\alpha_q \rho_q \vec{v}_q\right) + \nabla.\left(\alpha_q \rho_q \vec{v}_q \vec{v}_q\right) = -\alpha_q \nabla_p + \nabla.\bar{\bar{\tau}}_q + \alpha_q \rho_q \vec{g} + \sum_{p=1}^{n}\left(\vec{R}_{\mathrm{pq}} + \dot{m}_{\mathrm{pq}}\vec{v}_{\mathrm{pq}}\right). \tag{2}$$

The energy conservation formula is represented as

$$\frac{\partial}{\partial t}\left(\alpha_q \rho_q h_q\right) + \nabla.\left(\alpha_q \rho_q h_q \vec{u}_q\right) = \alpha_q \frac{\partial p_q}{\partial t} + \bar{\bar{\tau}}_q.\nabla\vec{u}_q - \nabla\vec{q}_q + S_q + \sum_{p=1}^{n}\left(Q_{\mathrm{pq}} + \dot{m}_{\mathrm{pq}}\vec{v}_{\mathrm{pq}}\right). \tag{3}$$

In the (SST) k-omega model, the kinetic energy which shows turbulence is governed by Hernandez et al. [32].

The kinematic eddy viscosity is calculated as

$$\nu_T = \frac{a_1 k}{\max\left(a_1\omega, SF_2\right)}. \tag{4}$$

The turbulence kinetic energy is

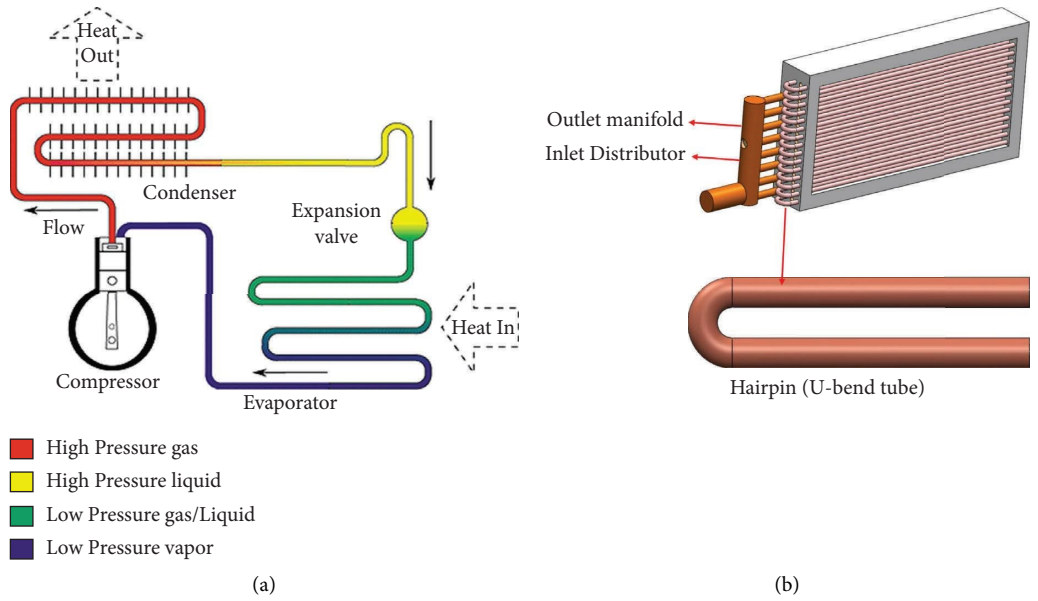

FIGURE 1: Schematic diagram of the vapor compression refrigeration (VCR) system: (a) basic system [37] and (b) evaporator heat exchanger with fins [38].

$$\frac{\partial k}{\partial t} + U_j \frac{\partial k}{\partial x_j} = P_k - \beta * k\omega + \frac{\partial}{\partial x_j}\left[\left(\nu + \sigma_k \nu_T\right)\frac{\partial k}{\partial x_j}\right]. \quad (5)$$

The specific dissipation rate is given by

$$\frac{\partial \omega}{\partial t} + U_j \frac{\partial \omega}{\partial x_j} = \alpha S^2 - \beta \omega^2 + \frac{\partial}{\partial x_j}\left[\left(\nu + \sigma_\omega \nu_T\right)\frac{\partial \omega}{\partial x_j}\right] + 2\left(1 - F_1\right)\sigma_{\omega 2}\frac{1}{\omega}\frac{\partial k}{\partial x_i}\frac{\partial \omega}{\partial x_i}. \quad (6)$$

The turbulent viscosity is calculated as

$$\mu_t = \rho C_\mu \frac{k^2}{\varepsilon}. \quad (7)$$

In the above equations, S_k and S_ϵ are the constant source terms, generally considered as zero, σ_k and σ_ϵ are the Prandtl turbulent numbers in terms of k and ϵ, where G_b and G_k are the kinetic energies for turbulence generating buoyancy and turbulence generating gradient speed, respectively, and Y_m is the dissipation rate of incompressible turbulence for dilution contribution.

The effectiveness of surface tension is explained by its force [42] as

$$F_\sigma = \sigma \frac{\sigma_l \rho_l k_l \nabla \alpha_l + \alpha_\nu \rho_\nu k_\nu \nabla \alpha_\nu}{(1/2)\left(\rho_l + \rho_\nu\right)}. \quad (8)$$

The calculated phases' interface curvature is

$$k_l = \nabla \frac{\nabla_{\alpha_l}}{|\nabla_{\alpha_l}|} \text{ and } k_\nu = \nabla \frac{\nabla_{\alpha_\nu}}{|\nabla_{\alpha_\nu}|}. \quad (9)$$

The energy equation and model together are represented as

$$\frac{\partial}{\partial t}(\rho E) + \nabla.\left[\vec{u}\left(\rho E + P\right)\right] = \nabla.\left(k \nabla T\right) + S_e. \quad (10)$$

The mixture of continuity is calculated as [32]

$$\frac{\partial(\rho_m)}{\partial t} + \nabla\left(\rho_m \vec{\nu}_m\right) = 0. \quad (11)$$

In the abovementioned equations, q is the heat flow, T_{wall} is the temperature of the tube wall, k is the thermal conductivity of the tube material, and d_i and d_o are the inside and outside diameters of the U-bend tube, respectively. ΔP_t and ΔP_a are the measured pressure and accelerating pressure, respectively, α is the void fraction, x is the vapor quality, ρ is the density, and G is the mass flux density. Again, ρ_m is the density of the mixture and $\vec{\nu}_m$ is the flow velocity [43] and the subscript k designates the mixed phase.

$$\vec{\nu}_m = \frac{\sum_{k=1}^{n} \varphi_k \rho_k \vec{\nu}_k}{\rho_m}, \qquad \rho_m = \sum_{k=1}^{n} \varphi_k \rho_k. \quad (12)$$

Combining the momentum equation for each phase gives the mixture momentum equation (32) as

$$\frac{\partial\left(\rho_m \vec{v}_m\right)}{\partial t} + \nabla\left(\rho_m \vec{v}_m \vec{v}_m\right) = -\nabla p + \nabla\left[\mu_m\left(\nabla \vec{v}_m + \nabla \vec{v}_m^T\right)\right] + \rho_m \vec{g} + \vec{F} + \nabla\left(\sum_{k=1}^{n}\left(\varphi_k \rho_k \vec{v}_{dr,k} \vec{v}_{dr,k}\right)\right). \tag{13}$$

The viscosity of the mixture is defined as follows:

$$\mu_m = \sum_{k=1}^{n} \varphi_k \mu_k. \tag{14}$$

The second phase drift velocity $\vec{v}_{dr,k}$ is defined by

$$\vec{v}_{dr,k} = \vec{v}_k - \vec{v}_m. \tag{15}$$

The energy equation is applied as follows:

$$\frac{\partial}{\partial t}\sum_{k=1}^{n}\left(\varphi_k \rho_k E_k\right) + \nabla \sum_{k=1}^{n}\left(\varphi_k \vec{v}_k\left(\rho_k E_k + P\right)\right) = \nabla\left(k_{eff} \nabla T\right) + S_E, \tag{16}$$

where $\vec{g}$ is defined as the acceleration due to gravity, n is the number of phases, μ_m is the viscosity of the mixture, E_k is the energy of each phase, T is the temperature, S_E includes the volumetric heat sources, and k_{eff} is the effective thermal conductivity.

The heat transfer coefficient equation (36) is assessed as

$$h = \frac{q}{\left(T_{\text{wall}} - T\right) - q\left(d_i/2k\right)\ln\left(d_o/d_i\right)}. \tag{17}$$

The measurement of the frictional pressure drop [36] is given by

$$\Delta P_r = \Delta P_t - \Delta P_a. \tag{18}$$

$$\Delta P_a = G^2\left\{\left(\frac{\left(1-x^2\right)^2}{\rho_l(1-a)} + \frac{x^2}{\rho_v \alpha}\right)_{out} - \left(\frac{\left(1-x^2\right)^2}{\rho_l(1-a)} + \frac{x^2}{\rho_v \alpha}\right)_{in}\right\}. \tag{19}$$

This study solves the numerical problem using a pressure-based solver by ANSYS Fluent, and the numerical setup with solver setting parameters is listed in Table 1, whereas Table 2 shows the boundary conditions.

2.3. Grid Independence Analysis and Validation. The meshing of the desired U-bend tube was performed by the commercial software ANSYS meshing. The inflation in mesh was developed to improve wall function and for better convergence. The meshing with tetrahedrons method is implemented along with patch confirmation here. The correctness of the numerical findings was confirmed by monitoring the total heat flux of the U-bend tube using a separate grid refinement test. The test outcomes revealed that the total heat flux remained unchanged when the percentage of elements well within the field declined by around 1.2%. Further grid refinement did not cause any noticeable changes to the total heat flux of the channel. Consequently, a grid system comprising 468314 elements and 177731 nodes was chosen for the calculation to lower the cost of computing, as additional cell increments would not affect the heat flux of the channel significantly. For a better understanding, the grid refinement test result is listed in Table 3.

The correctness of the computational model for two-phase heat transport was evaluated by utilizing experimental data from Oudah et al. [41]. The working fluid R134a was utilized for the purpose of validating the outcomes of this study. The experimental settings and geometric parameters were accurately reproduced in the numerical simulations. The findings exhibited a favorable concurrence between the experiment and CFD models, with a maximum discrepancy percentage error of 6.15%, as depicted in Figure 2(b). In addition, the graphs for both scenarios demonstrated comparable patterns. Again, Table 4 demonstrates the properties of R134a, R32, and R1234yf which will be useful for the analysis.

3. Results and Discussion

Numerical simulation was performed to investigate the evaporation of R32 and R1234yf with Al_2O_3 nanoparticles in a U-shaped tube, where the saturation temperature was maintained at 273.15 K. The simulations covered a mass flux range of 35–160 kg/m^2·s and vapor fractions ranging from 0.01 to 0.91 at the uniform temperature range from 300 K to 400 K.

3.1. U-Bend Analysis for R32 and R32-Al_2O_3

3.1.1. Mass Fluxes Effect of R32 and R32-Al_2O_3. In flow boiling evaporation of R32 and R32-Al_2O_3 in a U-bend tube with a downward flow, the mass flux and vapor fraction strongly influence the heat transfer coefficient. Figure 3 shows the variation of the heat transfer coefficient to vapor fraction by varying the mass flux from 35 to 160 kg/m^2·s at a constant temperature. The heat transfer coefficient decreases with increasing vapor fraction at a constant temperature through the upper straight section of the pipe. Due to a steady flow, the liquid refrigerant near the pipe wall takes the heat first, then vaporizes, and creates a vapor layer between the pipe wall and the remaining liquid. Consequently, there is a reduction in the heat flow from the pipe wall to the liquid, leading to a fall in the heat transfer coefficient. At the bend, the heat transfer coefficient increases slightly as a result of the separation of the flow and the change from stratified to annular flow. Hence, the convective heat transfer is enhanced. After the bend, the flow reverts

Table 1: Numerical setup with solver setting parameters and solution methods.

Parameter	Setup
Solver type	Pressure-based
Time	Steady
Velocity	Absolute
Model	Volume of fluid (VOF)*, mixture**
Phase	Multiphase (2)*, multiphase (3)**
Viscous model	SST k-omega model
Fluid	R32 and R1234yf with Al_2O_3
Mesh	Tetrahedron method
Pressure	PRESTO
Formulation	Explicit (R32), implicit (R1234yf)
Gradient	Least squares cell-based
Pressure-velocity coupling	SIMPLE

*R32 and R1234yf. **R32-Al_2O_3 and R1234yf-Al_2O_3.

Table 2: Boundary conditions.

Parameter	Setup/value
Type wall	Phase solid
Wall thickness	1.9 mm
Temperature	300–400 K
Inlet-boundary	
Type	Inflow
Phase	Multiphase (mixture)
Mass flux	35–160 kg/m^2·s
Inlet temperature	273 K
Gauge pressure	0.816 MPa
Outlet-boundary	
Type	Outflow

Table 3: Grid refinement test.

Node	Elements	Heat flux (kW/m^2·K)
177731	468314	1.511×10^2
258886	725618	1.511×10^2
349535	1019161	1.511×10^2

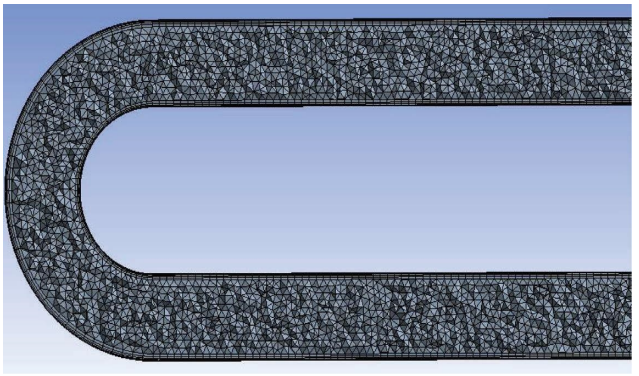

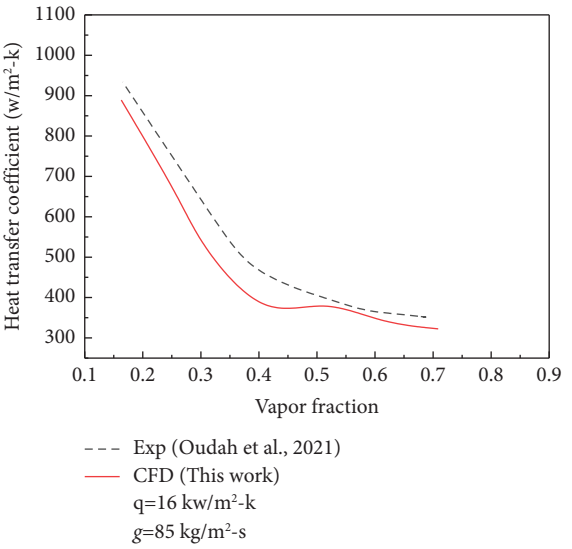

(a) (b)

Figure 2: Illustration of the grid independence test for the (a) mesh generation and (b) validation with experimental data [41].

Table 4: Properties of R32, R134a, and R1234yf [44–46] at T_{sat} = 273.15 K and P = 0.816, 0.2928, and 0.3158 MPa, respectively.

Properties	R134a		R32		R1234yf	
	Liquid	Vapor	Liquid	Vapor	Liquid	Vapor
Density (kg/m^3)	1294.8	14.428	1055	21.98	1176.3	17.64
Specific heat, Cp (J/kg·K)	1341	897.23	1745	1251	1289.3	926.18
Thermal conductivity (W/m·K)	0.0920	0.0115	0.1248	0.01284	0.0714	0.0116
Viscosity (kg/m·s)	0.000266	0.0000107	0.000124	0.00001228	0.000204	0.0000103
Molecular weight (kg/kmol)	102.03	102.03	52	52	114.04	114
Surface tension (N/m)	0.0114	0.0114	0.007	0.007	0.0094	0.0094

back to stratified flow, resulting in a further decrease in heat transmission. The trend observed in the illustrations for 300 K, 350 K, and 400 K is almost similar. At the given temperature of 300 K, as depicted in Figure 3(a), the heat transfer coefficient exhibits an upward trend owing to an augmentation in the mass flux. Eventually, it attains its peak value as a result of the substantial influence of forced convective evaporation, that is, at a mass flux of 160 kg/m^2·s. In Figures 3(b) and 3(c), it is shown that the heat transfer coefficients exhibit an increase when the temperatures are raised to 350 K and 400 K while maintaining the same mass flux. The vapor fraction has correspondingly augmented with the rise in temperature due to the enhanced transfer of heat to the liquid. The characteristics of vapor can be ascribed to a confluence of elements, encompassing convective boiling and nucleate contributions.

Figure 4 exhibits the effect of the heat transfer coefficient at different percentages of Al_2O_3 nanoparticles (0 vf% to 5 vf %) in the mixture with R32 refrigerant at a constant temperature of 350 K by varying the mass fluxes (60 kg/m^2·s, 85 kg/m^2·s, and 160 kg/m^2·s). Mixing Al_2O_3 nanoparticles with refrigerant R32 at different percentages certainly increased the heat transfer coefficient quite significantly, along with the vapor fraction, due to the higher heat conductivity of metal nanoparticles. From Figures 4(a) to 4(c), it can be seen that the heat transfer coefficients are increased for a constant temperature by increasing the mass fluxes and found its maximum values for nanoparticles at 5 vf%. However, the heat transfer coefficients are decreased with increasing the vapor fraction for all cases shown in the figures. Moreover, the heat transfer coefficient curves are characterized by a maximum point corresponding to the bent section of the tube. This happens because there is a flow separation and transition from stratified to annular flow that enhances the convective heat transfer coefficient. The shear forces imposed by the bend caused some shift flow pattern transition and bubble characteristics in the redeveloping flow section after the bend relative to the developed flow before the bend. The pressure gradient at the bend section increased with both vapor fraction and liquid superficial velocity and there was a sharp change in the pressure gradient profile during phase inversion. At low mixture velocity, pressure losses at the bend are higher than those in the straight sections [47, 48]. After the bend, the flow again becomes stratified, and the heat transfer continues to decrease. It is observed that the heat transfer coefficient increased by mixing 1% Al_2O_3 nanoparticle with the refrigerant R32 than with 0% Al_2O_3 nanoparticle. With further increases in nanoparticles' amount, the heat transfer coefficient increases sharply up to 3%. However, when the percentage of nanoparticles increases by more than 3%, the rising rate of the heat transfer coefficient starts to slow down.

3.1.2. Temperature Effect of R32. Figure 5 illustrates the impact of temperature on the overall heat transfer rate across different mass fluxes for the R32 refrigerant. As a consequence of the rise in temperature from 300 to 400 K, the mean heat transfer coefficient experiences an increase, reaching a threshold, due to the combined effects of convective boiling and nucleate contributions. There are noticeable variations in heat transfer coefficient and vapor fraction for the mass flux at 160 kg/m^2·s depicted in Figure 5(b) than the mass flux at 35 kg/m^2·s depicted in Figure 5(a). The observed fluctuations are explained by differences in refrigerant temperature along the boiling curve wall. The data presented in the figures indicate that when the temperature rises, there is an observed increase in both the vapor fraction and heat transfer coefficient, up to a specific threshold.

3.1.3. Frictional Pressure Drop of R32 and R32-Al_2O_3. Figure 6 demonstrates that the frictional pressure drop and the vapor quality increase as the mass fluxes increase from 35 to 160 kg/m^2·s at 300 K, 350 K, and 400 K, respectively. The frictional pressure drop was higher for the mass flow of 160 kg/m^2·s than for the smaller mass fluxes. An increase in mass flux results in a concurrent increase in resistive pressure drop. This can be attributed to the heightened contact shear stress between the liquid and vapor phases of R32, as well as between the two-phase fluid and the tube wall. Therefore, the shear stress is proportional to the resistive pressure of the mass flow. As temperature increases from 300 to 350 K, depicted in Figures 6(a) and 6(b), the frictional pressure drop increases for mass fluxes, increasing from 35 to 160 kg/m^2·s.

Comparably, the temperatures exhibited a rise from 350 to 400, depicted in Figures 6(b) to 6(c). The frictional pressure drop also increased by raising the mass fluxes from 35 to 160 kg/m^2·s. This is due to the density of the two phases of R32 decreasing, causing the vapor velocity to exceed that of the liquid film. This leads to higher shear stress and results in greater resistive pressure losses. The frictional pressure loss is much reduced because the liquid film is drastically reduced at the higher vapor fraction. Since the fluid has been receiving more heat, the vapor

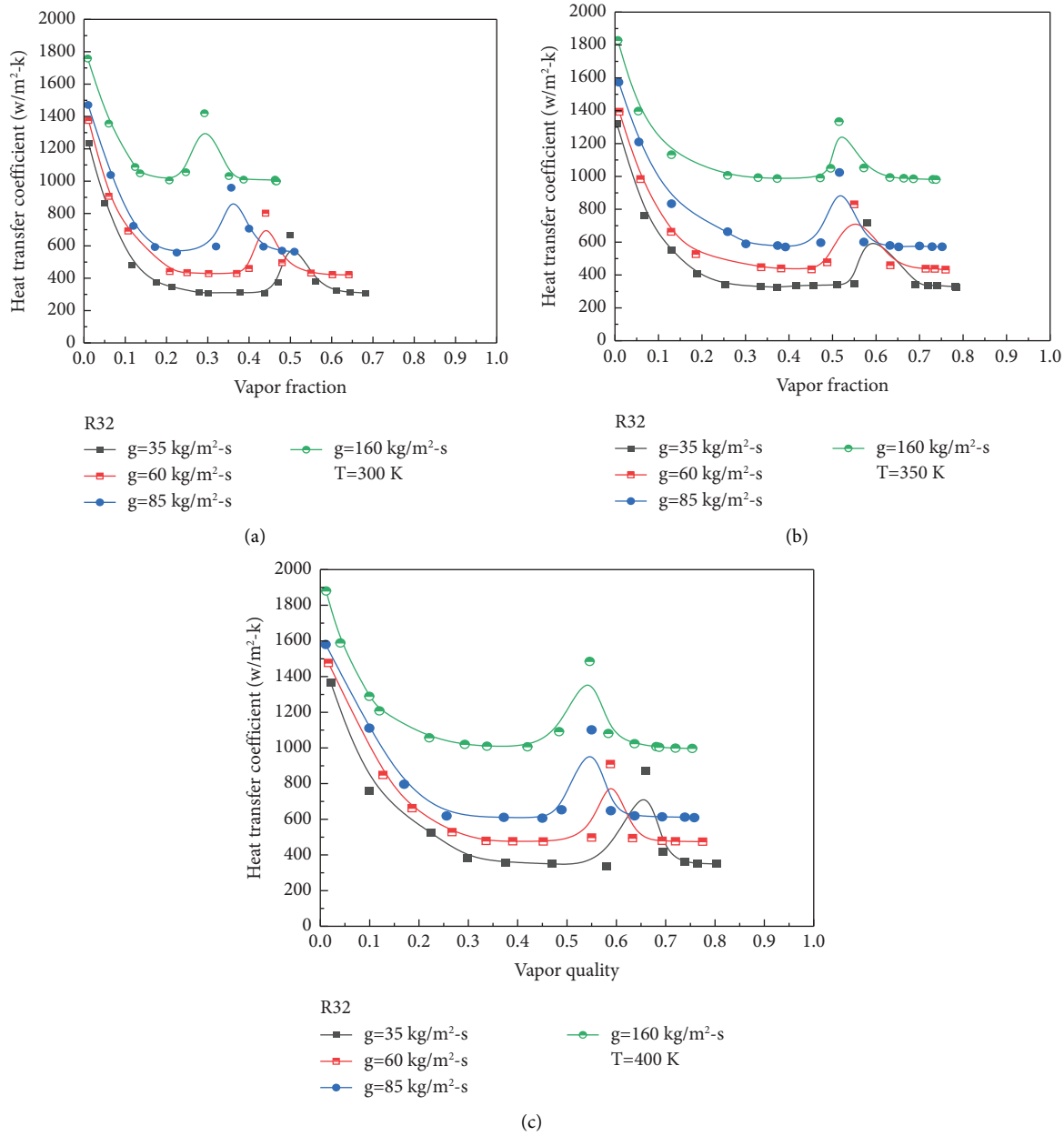

Figure 3: Variation of heat transfer coefficient for vapor fraction of R32 at various mass fluxes at (a) 300 K, (b) 350 K, and (c) 400 K.

fractions have similarly increased with temperature. Moreover, frictional pressure drop also increased significantly over the vapor fraction for the higher mass fluxes and the temperature increments.

Again, Figure 7 resembles the resistive pressure drop and the vapor quality for different percentages (0 to 5%) of Al_2O_3 nanoparticles with R32 at a constant temperature of 350 K by varying the mass fluxes from 60 to 160 kg/m^2·s mass flux. Mixing the Al_2O_3 nanoparticles with the R32 at 1% percentage increases the frictional pressure drop slightly than the 0% nanoparticles mixture. This is due to the density of the two phases of R32-Al_2O_3 nanofluid decreasing, causing the vapor velocity to exceed that of the liquid film. This leads to higher shear stress and results in greater resistive pressure losses. Further increasing the amount of the nanoparticles to up to 3%, the frictional pressure drop increases but not quite significantly. Using the various mass fluxes (60, 85, and 160 kg/m^2·s) on different percentages of Al_2O_3 nanoparticles with R32 at a constant temperature of 350 K, the resistive pressure drop increased due to an increase in the contact shear stress between the R32-Al_2O_3 nanofluid liquid and vapor phases as well as the two-phase fluid and the tube wall.

3.1.4. Flow Formation of R32 and R32-Al_2O_3. The velocity vector and streamline were obtained at a mass flux of 160 kg/m^2·s and at a temperature of 350 K, in order to analyze the improved performance of the heat transfer coefficient, temperature effect, and frictional pressure drop for R32 and

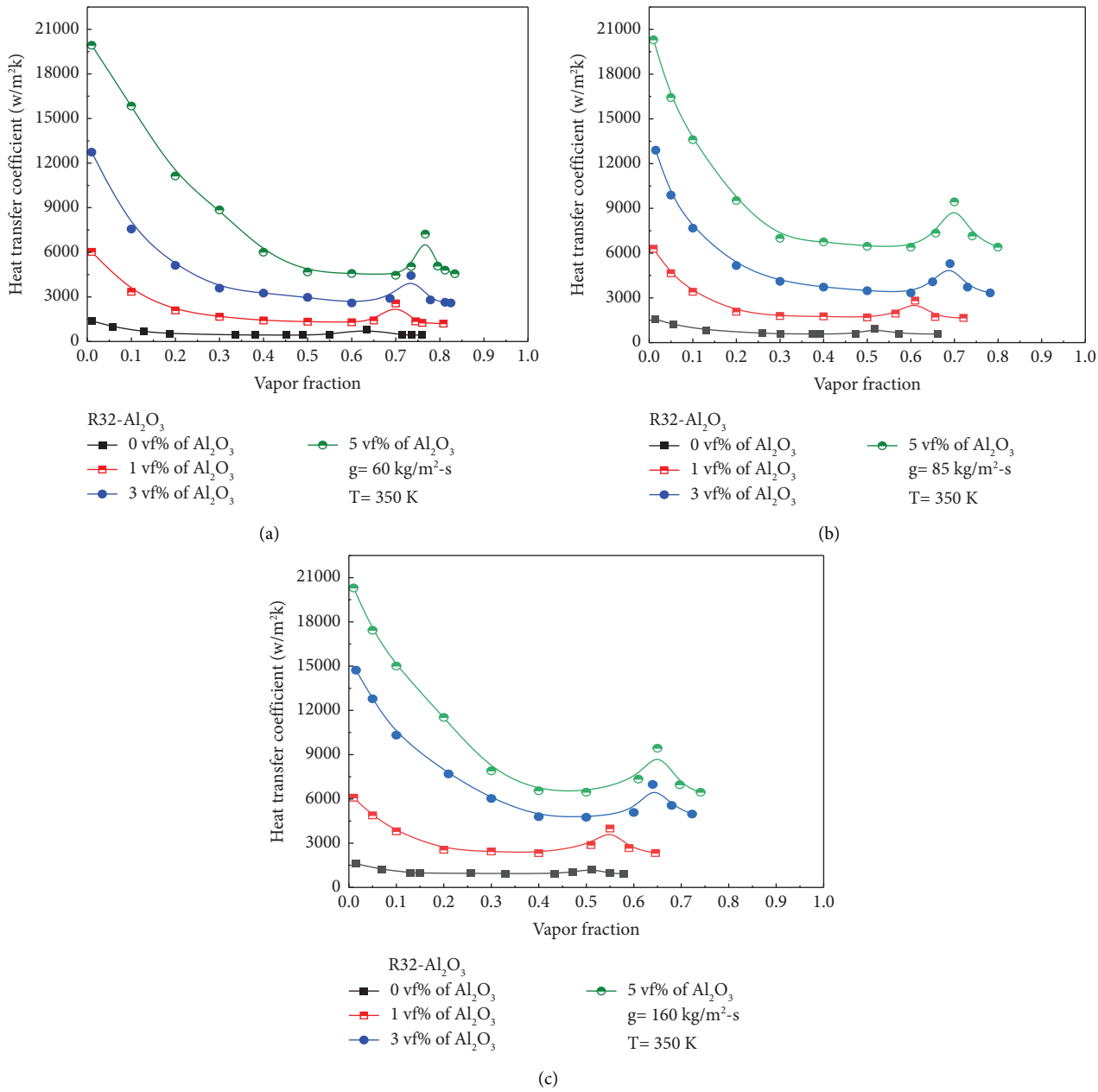

Figure 4: Variation of heat transfer coefficient at a constant temperature for different percentages of R32-Al_2O_3 nanofluid at various mass fluxes of (a) 60 kg/m^2·s, (b) 85 kg/m^2·s, and (c) 160 kg/m^2·s.

R32-Al_2O_3. Figures 8 and 9 exhibit the velocity vector and velocity streamline, respectively, to identify the flow pattern of the liquid and vapor mixture of R32 and R32-Al_2O_3 in a U-bend tube at 160 kg/m^2·s mass flux and at a temperature of 350 K. Figure 8(a) illustrates the velocity vector of R32 for the liquid and vapor phases that identifies the liquid film thickness and the interfacial area between the liquid and vapor phases depending on the flow velocity and affects the heat transfer area. In Figure 8(b), the velocity streamlines of R32 refrigerant for the liquid and vapor phases are indicated where the streamlines are parallel to the axis of the pipe and provide a visualization of the velocity distribution at any given moment in time.

In contrast, Figure 9(a) illustrates the velocity vector of the R32-Al_2O_3 nanofluid that serves to characterize the liquid film thickness and the interfacial area between the liquid and vapor phases. Conversely, Figure 9(b) depicts the velocity streamline of the R32-Al_2O_3 nanofluid, specifically highlighting the behavior of the liquid and vapor phases. The velocity streamlines exhibit a parallel orientation to the axis of the pipe, thus serving as a means to visually represent the distribution of velocity at a specific instant in time.

Moreover, Figure 10 illustrates the flow pattern development during the flow boiling evaporation of R32 within a U-bend tube. The evaporation starts from the adjacent

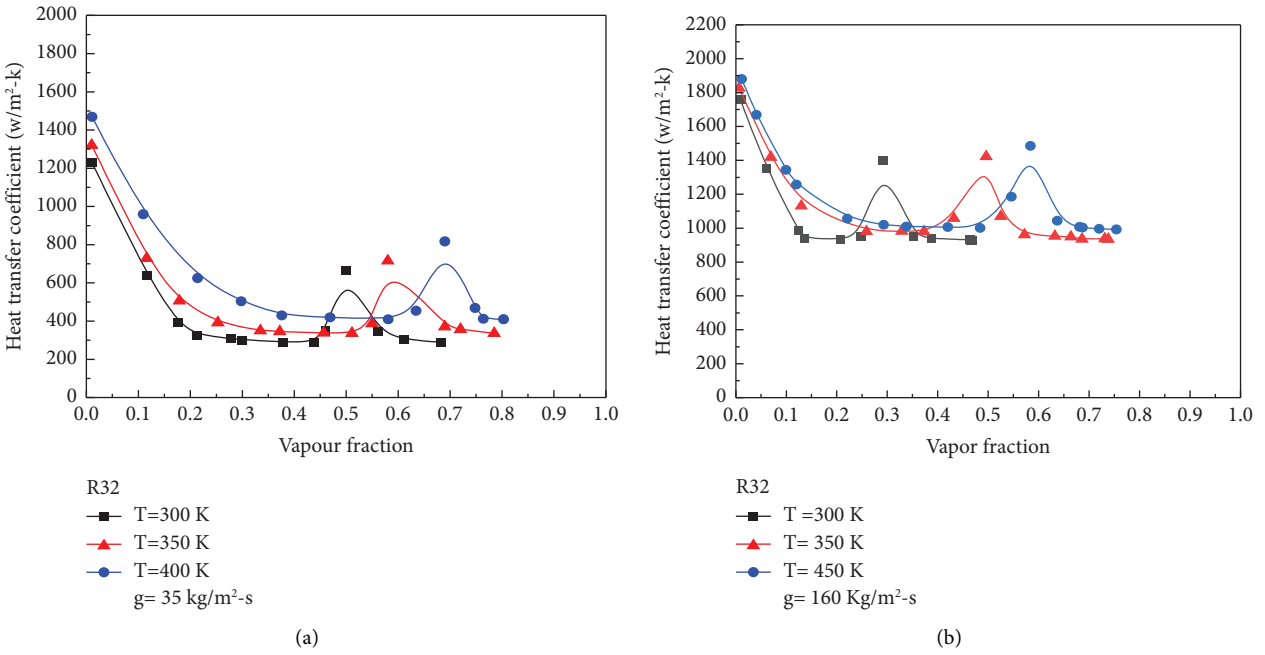

Figure 5: Variation of heat transfer coefficient for vapor fraction of R32 at various temperatures and at mass fluxes of (a) 35 kg/m^2·s and (b) 160 kg/m^2·s.

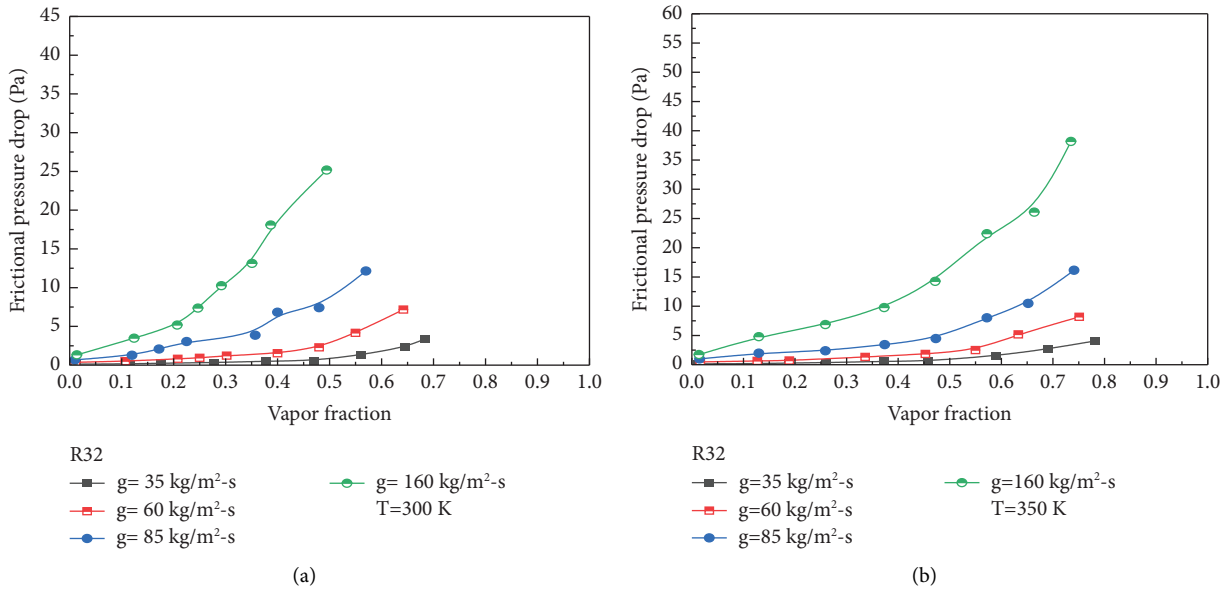

Figure 6: Continued.

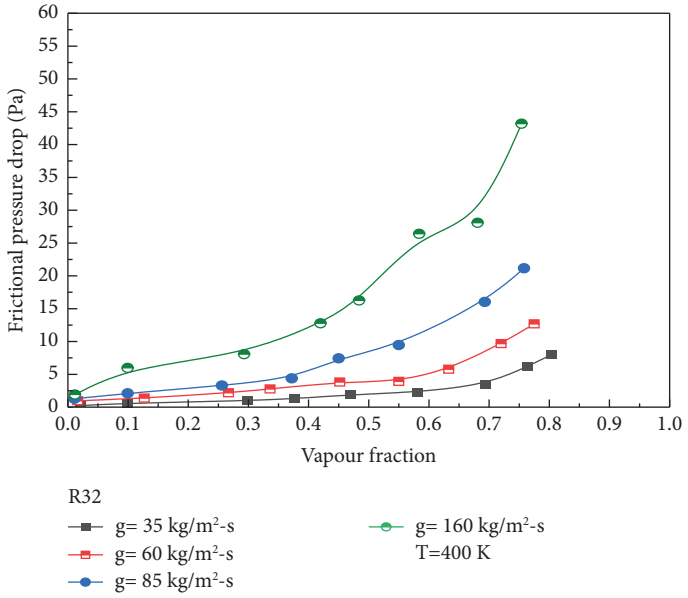

(c)

Figure 6: Variation of frictional pressure drop for vapor fraction of R32 at various mass fluxes and at temperatures of (a) 300 K, (b) 350 K, and (c) 400 K.

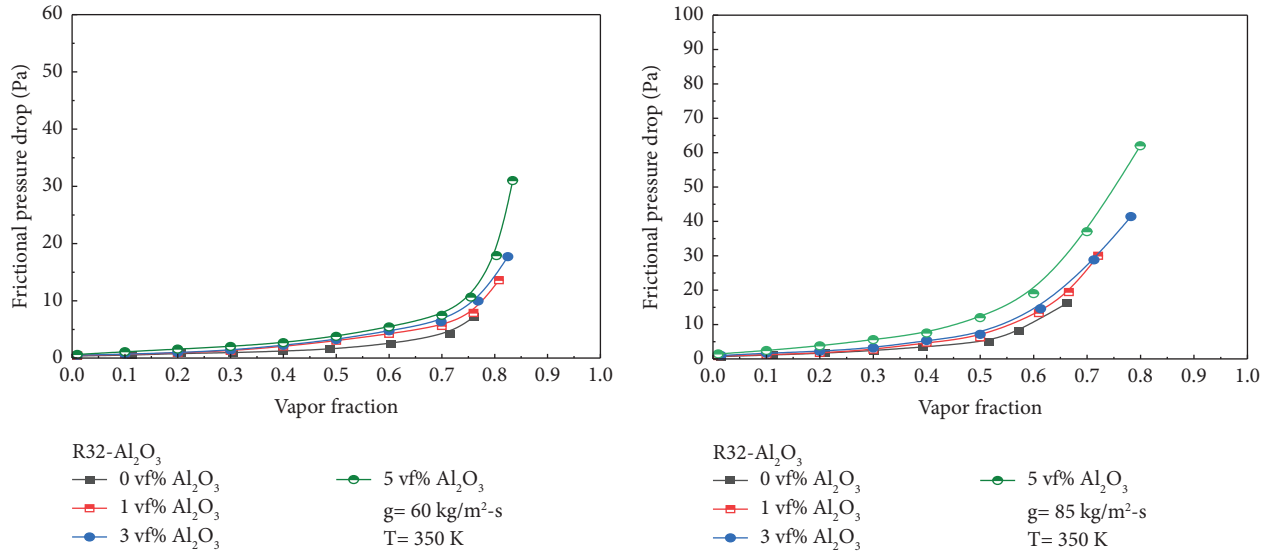

(a) (b)

Figure 7: Continued.

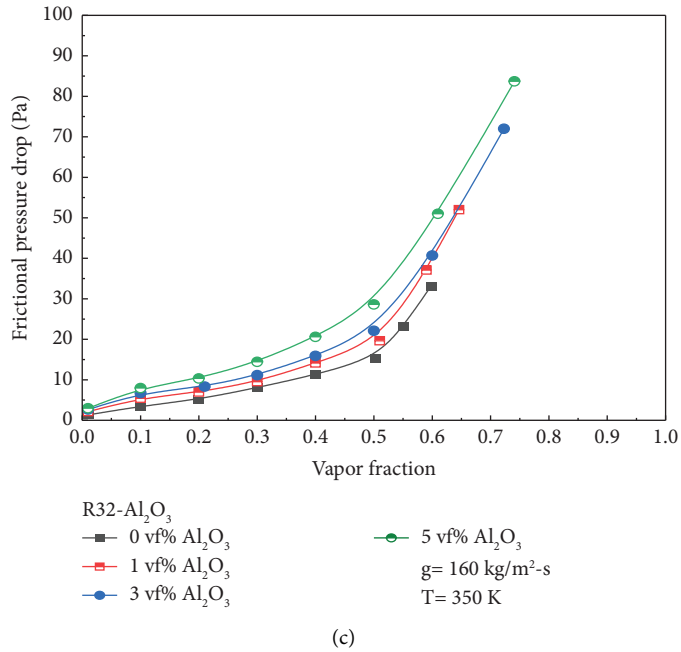

Figure 7: Variation of frictional pressure drop at constant temperature for different percentages of R32-Al_2O_3 nanofluid at various mass fluxes of (a) 60 kg/m^2·s, (b) 85 kg/m^2·s, and (c) 160 kg/m^2·s.

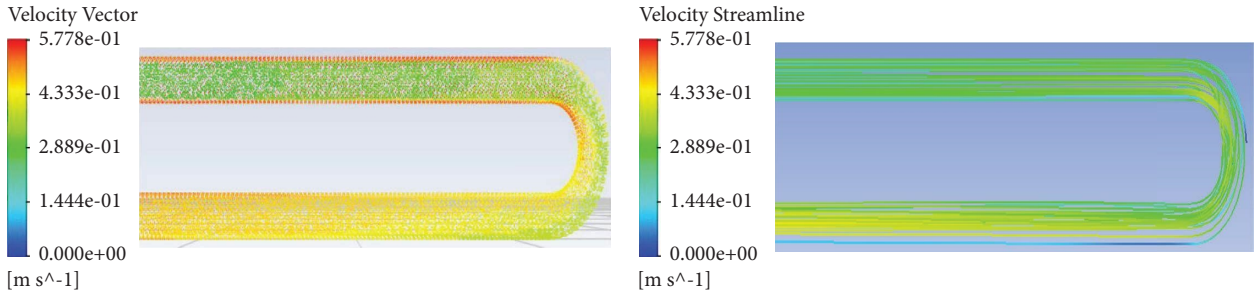

Figure 8: Illustration for the (a) velocity vector and (b) velocity streamline of multiphase flow for R32 at 160 kg/m^2·s of mass flux at 0.01 vapor fraction and at 350 K temperature.

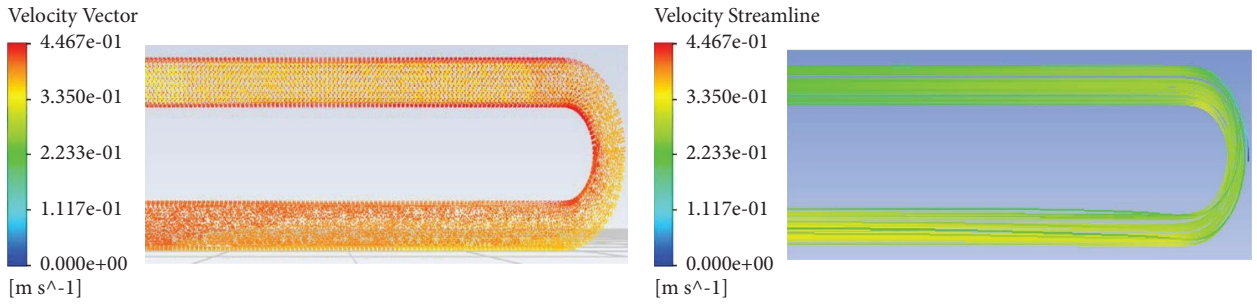

Figure 9: Illustration of the (a) velocity vector and (b) velocity streamline of multiphase flow for R32-Al_2O_3 nanofluid at 160 kg/m^2·s of mass flux at 0.01 vapor fraction and at 350 K temperature.

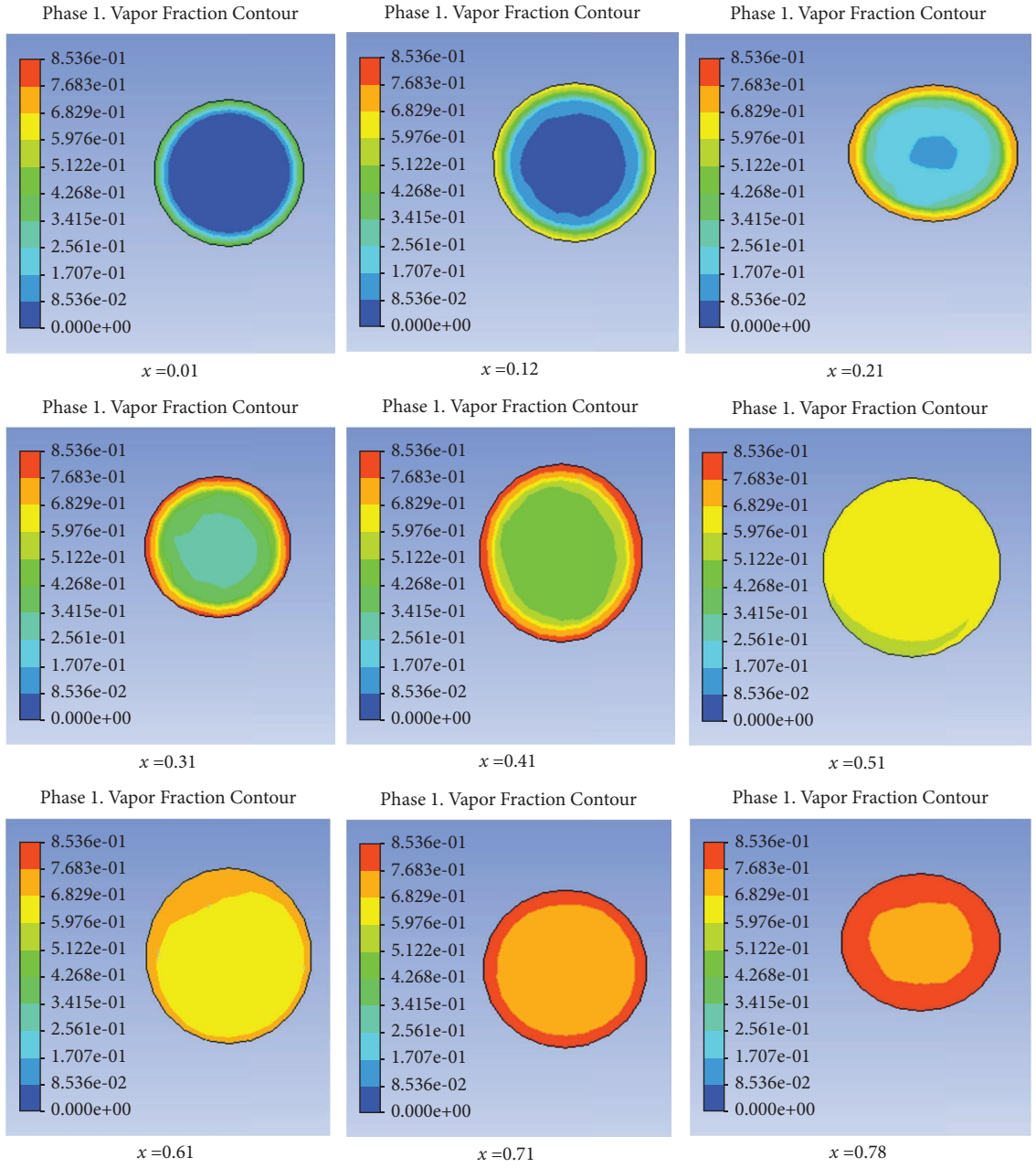

Figure 10: Flow formation for R32 and vapor quality within 0.01~0.78 occurred before the bend ($x = 0.01$ to 0.41), at the bend ($x = 0.51$ to 0.61), and after the bend ($x = 0.71$ to 0.78) and at the mass flux of 160 kg/m^2·s and at the temperature of 350 K.

liquid of the tube wall, and a vapor layer forms around the pipe wall. As the mixture of liquid and vapor moves along the pipe, the vapor layer also grows in thickness. At the bend section, fluid and vapor mixture passing through the bend is affected by various forces, such as centrifugal force, density differences between phases, buoyancy forces, viscous forces, and gravitational forces. These forces cause secondary flows that alter the path of the fluid, resulting in a redistribution of the phases at the bend. As a result, the vapor fraction increasing rate accelerated. It is shown that the flow formation of flow boiling evaporation occurred for the R32 refrigerant at the vapor fractions from 1% to 78% through the U-bend pipe.

Figure 11 shows the flow formation of flow boiling evaporation of R32-Al_2O_3 nanofluid from a vapor fraction of 1% to a vapor fraction of 83% in a U-bend tube. The evaporation starts at a faster rate than R32 from the adjacent liquid of the tube wall at 350 K temperature. After mixing the Al_2O_3 nanoparticles with R32, the vapor fraction increased from 78% to 83%.

3.2. U-Bend Analysis for R1234yf and R1234yf-Al_2O_3

3.2.1. Mass Flux Effect of R1234yf and R1234yf-Al_2O_3. Figure 12 resembles the effect of mass fluxes variation from 60 to 160 kg/m^2·s at a constant temperature on the heat

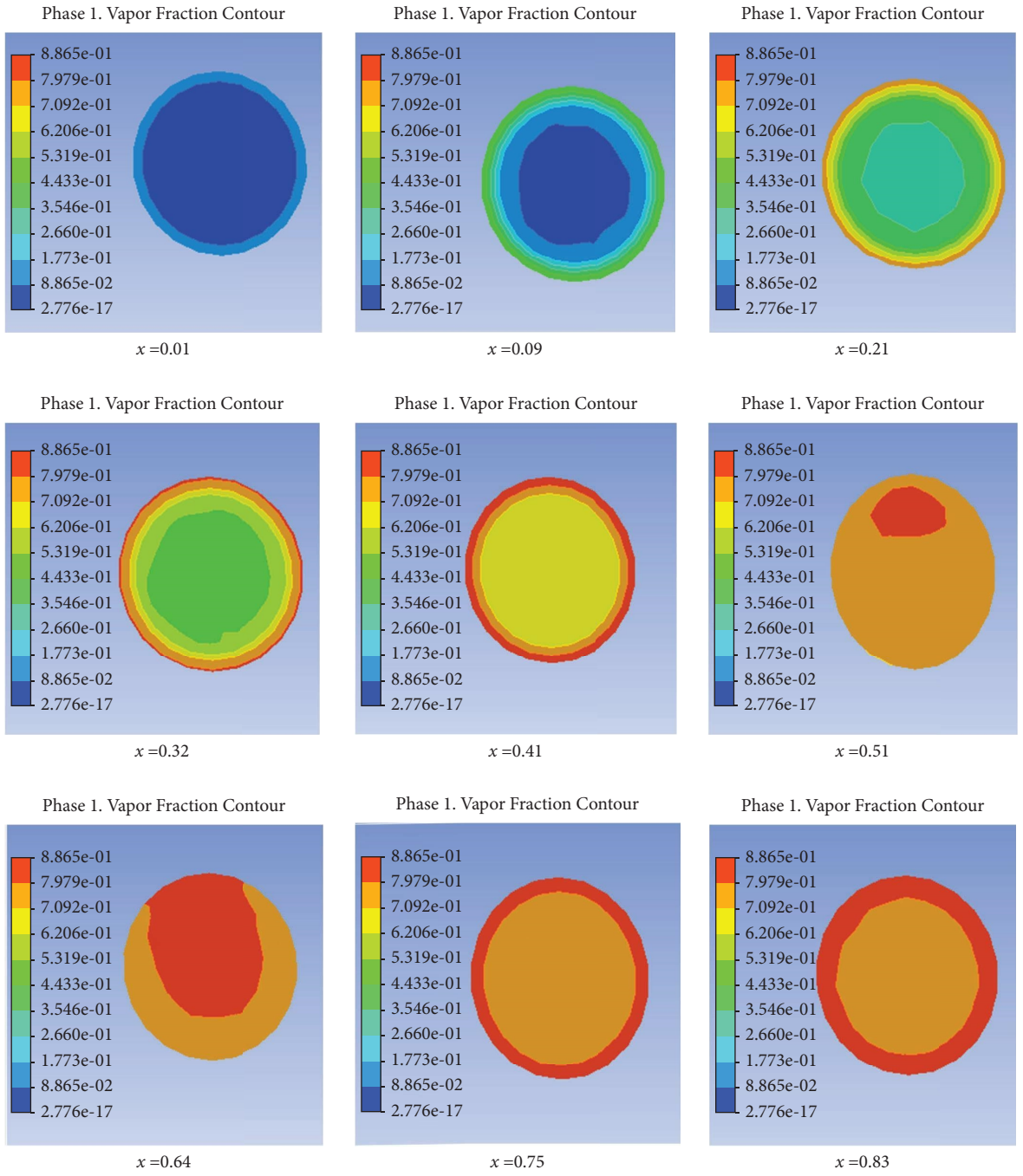

Figure 11: Flow formation for R32-Al_2O_3 nanofluid and quality within 0.01~0.83 occurred before the bend ($x = 0.01$ to 0.41), at the bend ($x = 0.51$ to 0.64), and after the bend ($x = 0.75$ to 0.83) at the mass flux of 160 kg/m^2·s and at the temperature of 350 K.

transfer coefficient. At the beginning of the flow, the heat transfer coefficient decreases through the upper straight section of the pipe at a fixed temperature. Due to the steady flow, the liquid near the pipe wall takes the heat first and vaporizes and creates a vapor layer between the pipe wall and the remaining liquid. Consequently, there is a reduction in the heat flow from the pipe wall to the liquid, leading to a fall in the heat transfer coefficient. Subsequently, the decreasing rate of heat transfer begins to slow down. At the bend, there is a discernible augmentation in the process of heat transfer. The observed phenomenon can be attributed to the occurrence of flow separation and the subsequent change from stratified flow to annular flow, which leads to an augmentation of convective heat transfer. After the bend, the fluid motion once again assumes a stratified flow pattern.

Moreover, Figures 12(a) and 12(b) demonstrate that the heat transfer coefficients exhibit an increase when the temperature is raised from 300 to 350 K at the same mass flux. The vapor fractions have correspondingly augmented with the rise in temperature due to the enhanced transfer of heat to the liquid. Figure 12(c) illustrates the mean heat transfer coefficient at a temperature of 400 K across various

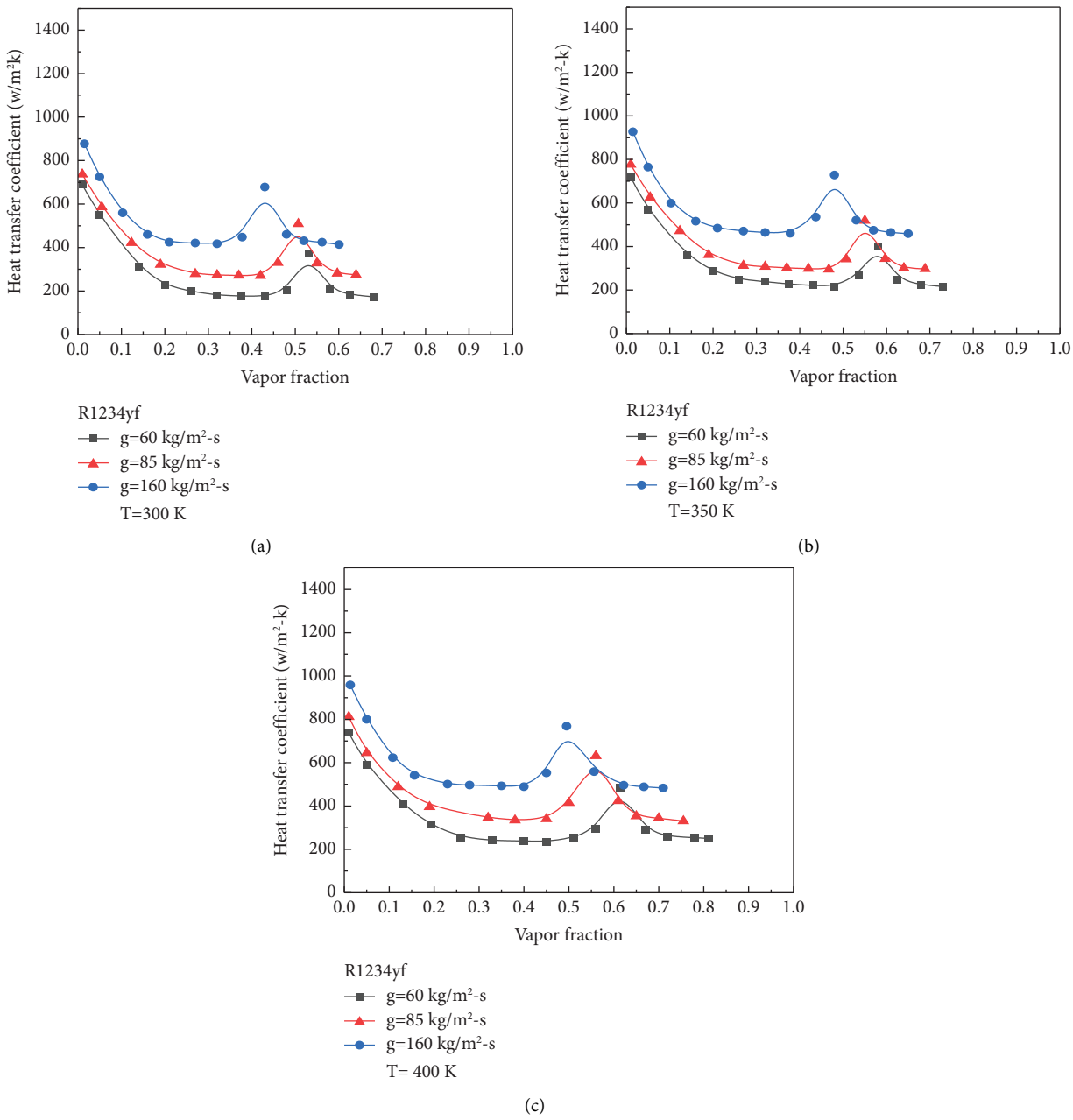

Figure 12: Variation of heat transfer coefficient for vapor fraction of R1234yf at various mass fluxes and at the temperatures of (a) 300 K, (b) 350 K, and (c) 400 K.

mass fluxes. The heat transfer coefficient exhibits an increase until it reaches a specific threshold, which can be attributed to the rise in temperature up to 400 K. At a mass flux of 160 kg/m^2·s, the heat transfer coefficient reaches its highest value as a result of the substantial influence of forced convective evaporation.

Figure 13 shows the effect of the heat transfer coefficient at different percentages (0 to 5%) of Al_2O_3 nanoparticles with R1234yf refrigerant at a constant temperature of 350 K on the 60–160 kg/m^2·s mass fluxes. Mixing nanoparticles with the refrigerant at different percentages certainly increased the heat transfer coefficient, whereas 1% of Al_2O_3 nanoparticles with refrigerant R1234yf increased the heat transfer coefficient close to 4 times more than that of 0% nanoparticles. Further increases in nanoparticles amount up to 3%, and the heat transfer coefficient also increased around 2 times than 1% mixture of nanoparticles with the refrigerant. When the percentage of Al_2O_3 nanoparticles is at 5%, the heat transfer coefficient is at its maximum value. However, when the percentage of nanoparticles increases by more than 3%, the rate of increasing the heat transfer coefficient is only 50.8% because a higher percentage of nanoparticles hampers the flow rate of refrigerants. Figures 13(a) and 13(b) show that increasing the mass flux from 60 kg/m^2·s to 85 kg/m^2·s also increased the heat transfer coefficient to 32%. While Figure 13(c) shows the

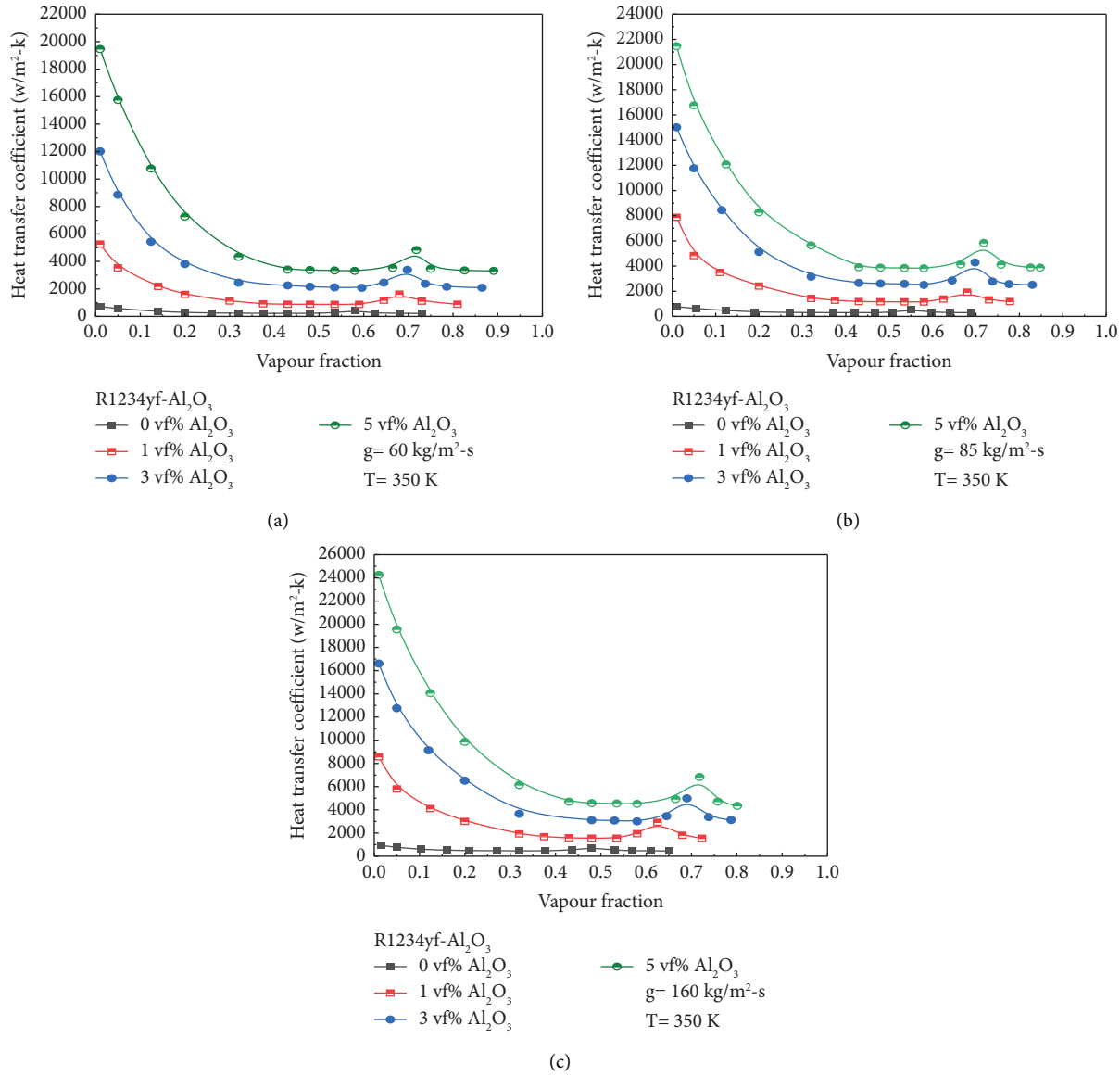

FIGURE 13: Variation of heat transfer coefficient at constant temperature for different percentages of Al_2O_3-R1234yf nanofluid at various mass fluxes of (a) 60 kg/m^2·s, (b) 85 kg/m^2·s, and (c) 160 kg/m^2·s.

34% more heat transfer coefficient at a mass flux of 160 kg/m^2.s than the heat transfer coefficient encountered by the mass flux 85 kg/m^2.s in Figure 13(b).

3.2.2. Temperature Effect of R1234yf. Figure 14 shows the temperature effects on the overall heat transfer rate for R1234yf at constant mass fluxes. The heat transfer coefficient is increased by 35.04% at the mass flux of 60 kg/m^2·s, shown in Figure 14(a), while 19% at the mass flux of 85 kg/m^2·s, shown in Figure 14(b) as temperature increases from 300 K to 400 K and vapor fraction also increased. Again, Figure 14(c) indicates the temperature effect on the same mass flux of 160 kg/m^2·s, where the 26% heat transfer coefficient has increased as the temperature rises from 300 K to 400 K. These differences are related to the boiling curve's wall refrigerant temperature disparities.

3.2.3. Frictional Pressure Drop of R1234yf and R1234yf-Al_2O_3. Figure 15 shows that the frictional pressure drop of R1234yf increases along with the vapor quality as the mass fluxes increase from 60 to 160 kg/m^2·s at the constant temperatures of 300 K, 350 K, and 400 K, respectively. As mass flux increases, the frictional pressure drop increases with increasing vapor fraction. From Figure 15(a), the frictional pressure drop was found to be more than 2 times higher at 160 kg/m^2·s than at 60 kg/m^2·s of mass flux. The resistive pressure drop increased as the mass flux increased due to an increase in the contact shear stress between the R1234yf liquid and vapor phases as well as the two-phase fluid and the tube wall. As a result, the resistive pressure for mass flow is proportional to the shear stress. For 85 kg/m^2·s at 350 K, shown in Figure 15(b), the frictional pressure drop is 64.5% higher than the same mass flux at 300 K. This is due to the density of the two phases of R1234yf decreasing,

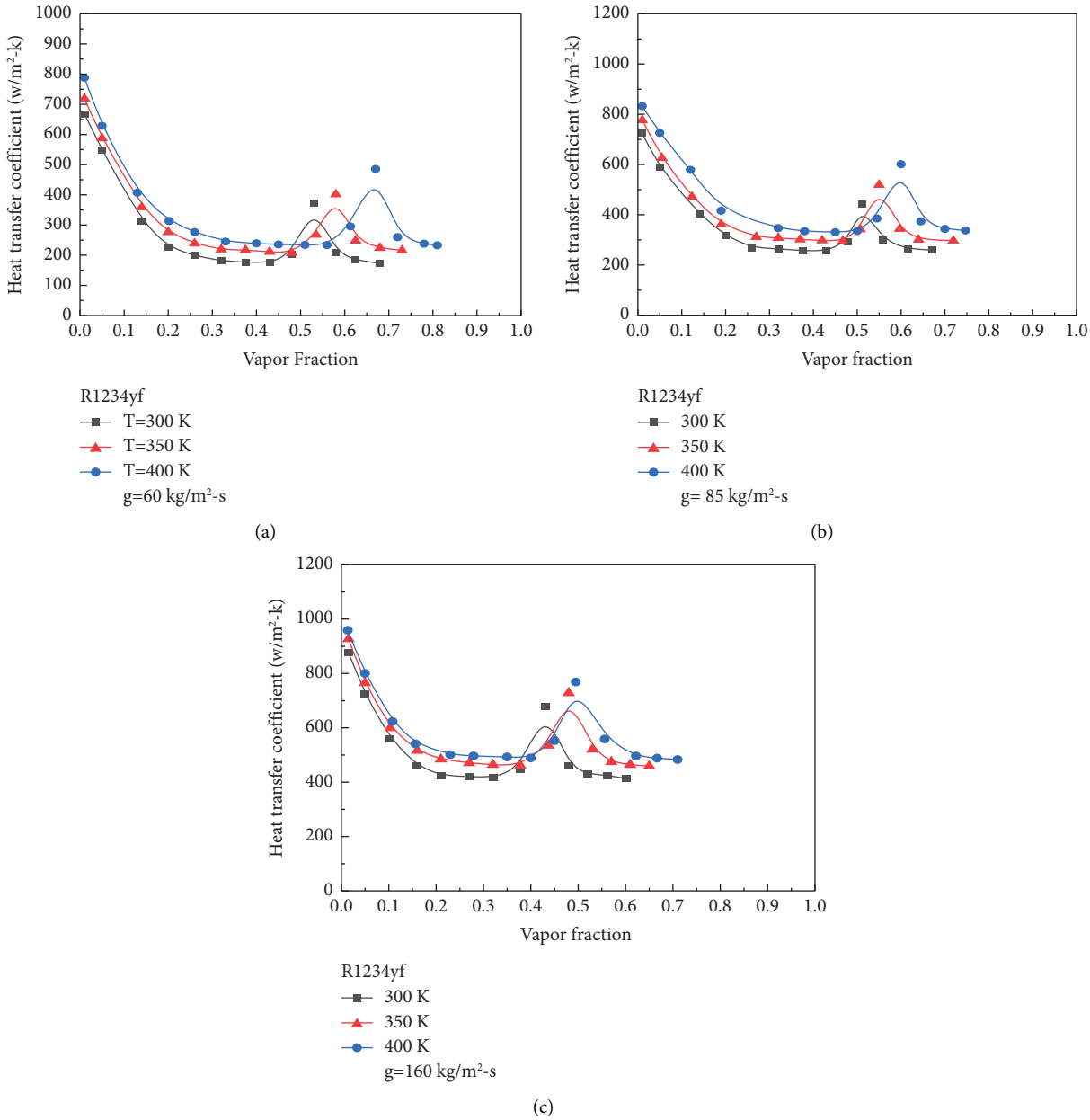

Figure 14: Variation of heat transfer coefficient for vapor fraction of R1234yf at various temperatures and at various mass fluxes of (a) 60 kg/m^2·s, (b) 85 kg/m^2·s, and (c) 160 kg/m^2·s.

causing the vapor velocity to exceed that of the liquid film. This leads to a higher shear stress and results in greater resistive pressure losses. The frictional pressure drop is much reduced because the liquid film is drastically reduced at higher vapor quality. Figure 15(c) shows the highest pressure drop as the temperature increases from 350 to 400 K and the frictional pressure drop also becomes double at a constant mass flux of 160 kg/m^2·s.

In contrast, Figure 16 shows that the frictional pressure drop increases along with the quality of the vapor at a constant temperature of 350 K for different percentages (0 to 5%) of Al_2O_3 nanoparticles with R1234yf at mass fluxes of 60, 85, and 160 kg/m^2·s, respectively. By mixing the Al_2O_3 nanoparticles with the R1234yf at 1% percentage, the frictional pressure drop increases by 43% more than the 0% nanoparticles mixture. This is due to the density of the two phases of R1234yf-Al_2O_3 nanofluid decreasing, causing the vapor velocity to exceed that of the liquid film. This leads to a higher shear stress and results in greater resistive pressure losses. By further increasing the nanoparticles to up to 3%, the frictional pressure drop increases to 58.71%. Moreover, 5% nanoparticles with R1234yf show the highest frictional pressure drop. When the mass flux rises from 85 kg/m^2·s to 160 kg/m^2·s, shown in Figures 16(b) and 16(c), the resistive pressure drop increases due to an increase in the contact shear stress between the R1234yf-Al_2O_3 nanofluid liquid and vapor phases as well as the two-phase fluid and the tube wall.

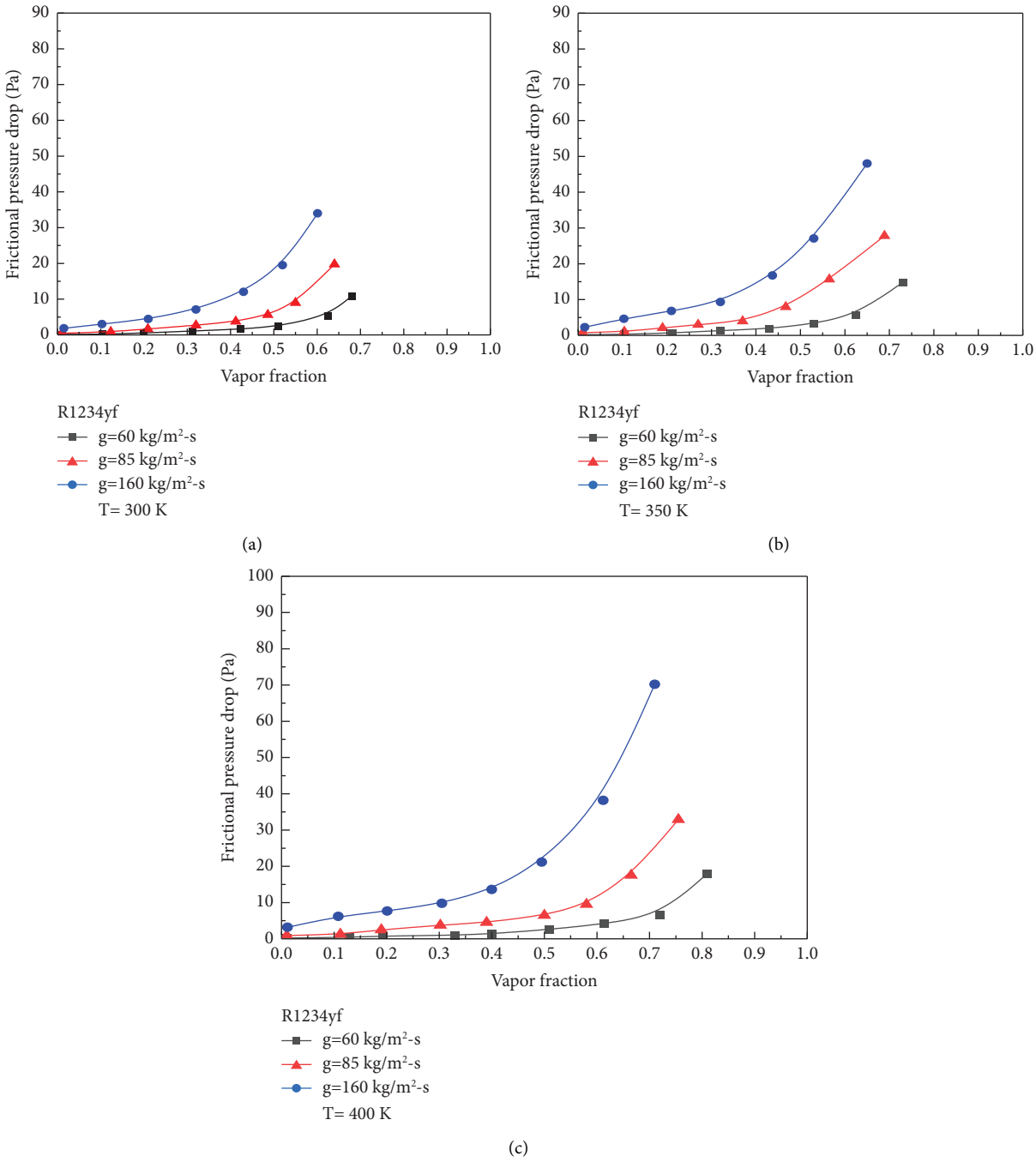

Figure 15: Variation of frictional pressure drop for vapor fraction of R1234yf at various temperatures of (a) 300 K, (b) 350 K, and (c) 400 K.

3.2.4. Flow Formation of R1234yf and R1234yf-Al_2O_3. In accordance with better performance of heat transfer, temperature effect, and frictional pressure drop of R1234yf and R1234yf-Al_2O_3 nanofluid at 160 kg/m^2·s mass flux and at 350 K temperature, the velocity vector and streamline are taken at 160 kg/m^2·s mass flux and at 350 K temperature. Figures 17 and 18 show the velocity vector and velocity streamlines of evaporation for R1234yf and R1234yf-Al_2O_3 in a U-bend tube. Figure 17(a) indicates the velocity vector of R1234yf for the liquid and vapor phases that identifies the liquid film thickness and the interfacial area between the liquid and vapor phases depending on the flow velocity and affects the heat transfer area, while Figure 17(b) exhibits the velocity streamlines of R1234yf refrigerant for the liquid phase and vapor phase mixture. The velocity streamlines are parallel to the axis of the pipe and provide a visualization of the velocity distribution at any given moment in time.

In contrast, Figure 18(a) indicates the velocity vector of R1234yf-Al_2O_3 nanofluid for the liquid phase and vapor phase that identifies the liquid film thickness and the interfacial area between the liquid and vapor phases depending on the flow velocity and affects the heat transfer area. In

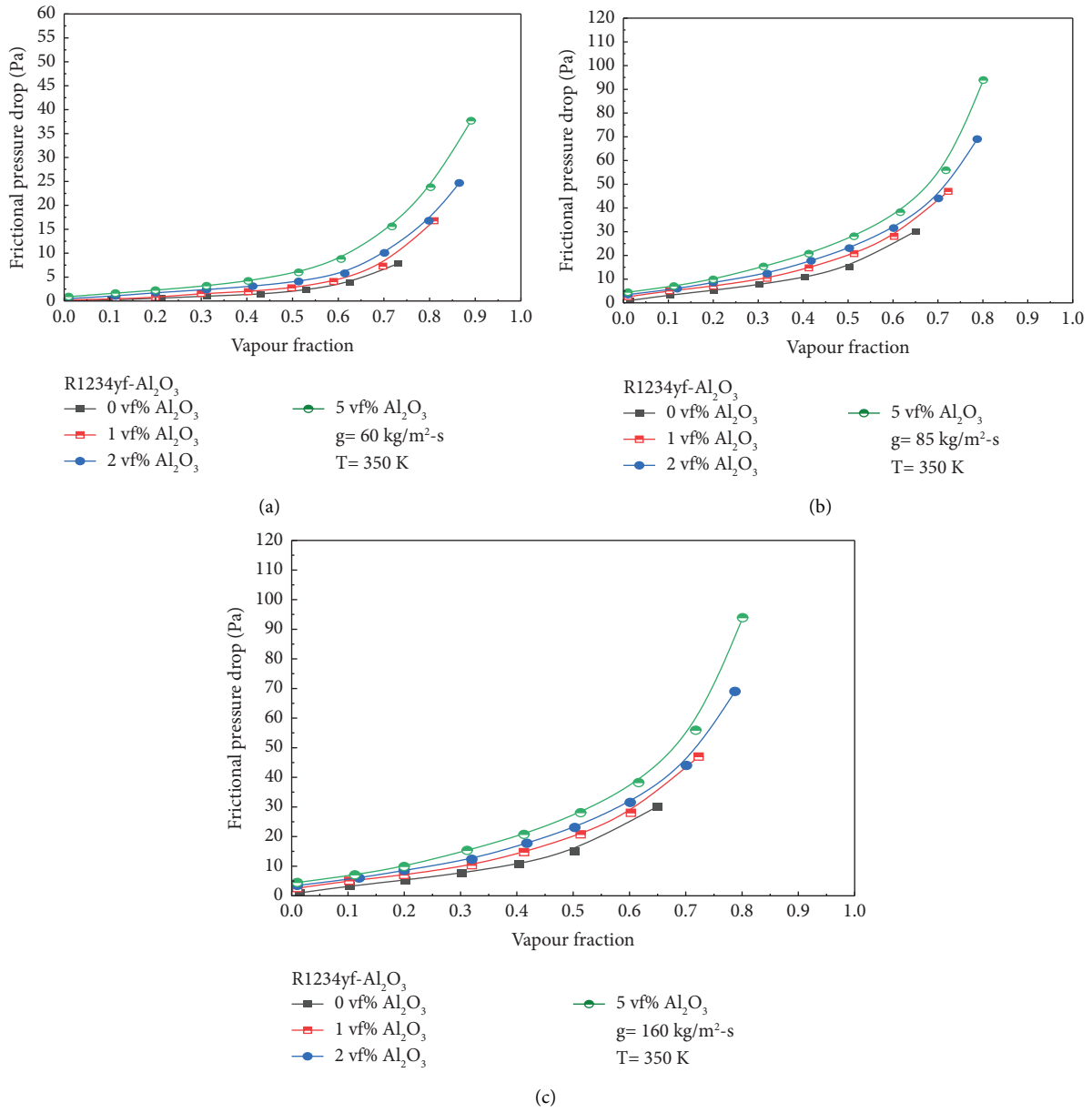

Figure 16: Variation of frictional pressure drop at constant temperature for different percentages of R1234yf-Al_2O_3 nanofluid at various mass fluxes of (a) 60 kg/m^2·s, (b) 85 kg/m^2·s, and (c) 160 kg/m^2·s.

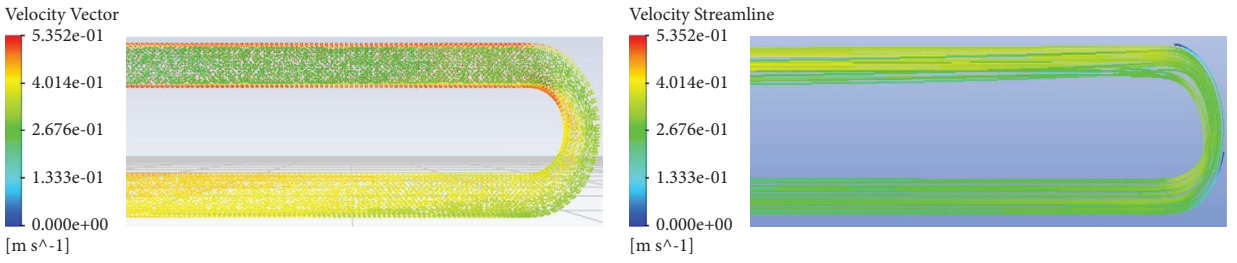

Figure 17: Illustration for the (a) velocity vector and (b) velocity streamline of multiphase flow for R1234yf at 160 kg/m^2·s of mass flux at 0.01 vapor fraction and at 350 K temperature.

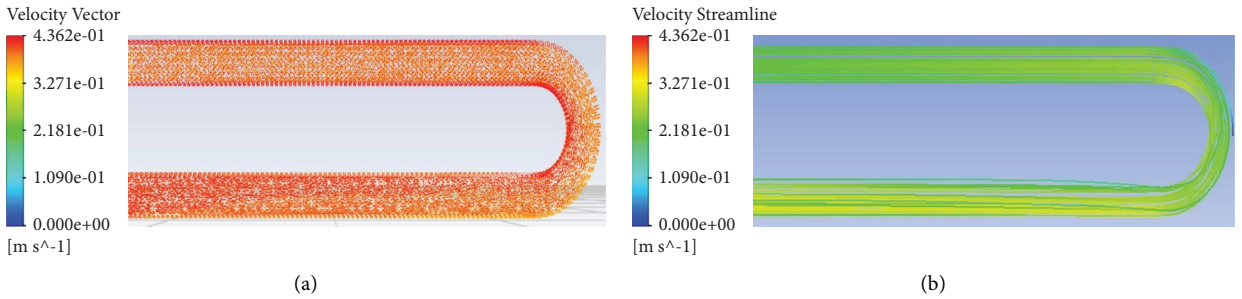

(a) (b)

FIGURE 18: Illustration for the (a) velocity vector and (b) velocity streamline of multiphase flow for R1234yf-Al_2O_3 at 160 kg/m^2·s of mass flux at 0.01 vapor fraction and at 350 K temperature.

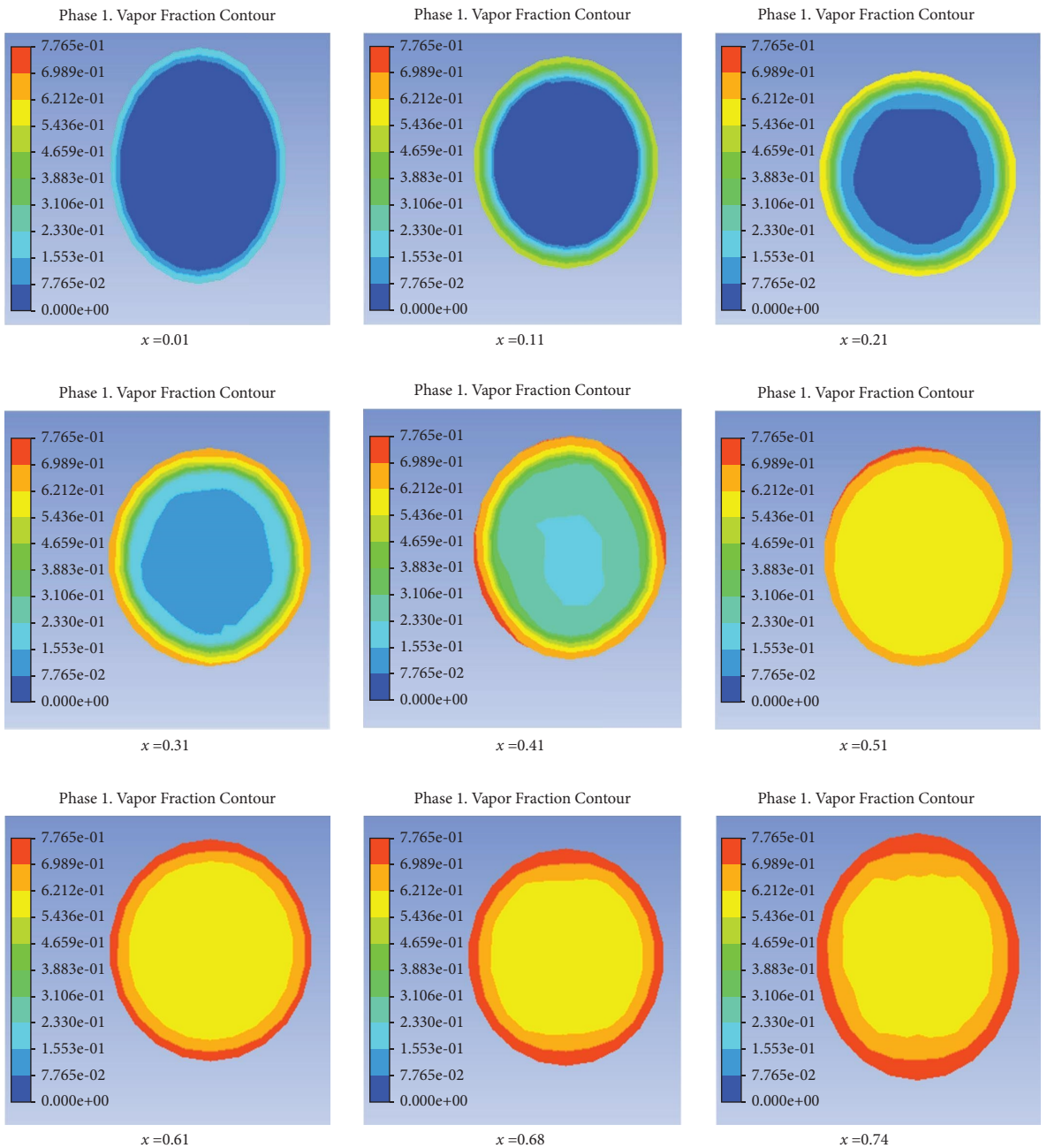

FIGURE 19: Flow formation for R1234yf and vapor quality within 0.01~0.74 occurred before the bend ($x = 0.01$ to 0.41), at the bend ($x = 0.51$ to 0.61), and after the bend ($x = 0.68$ to 0.74) at the mass flux of 160 kg/m^2·s and at temperature of 350 K.

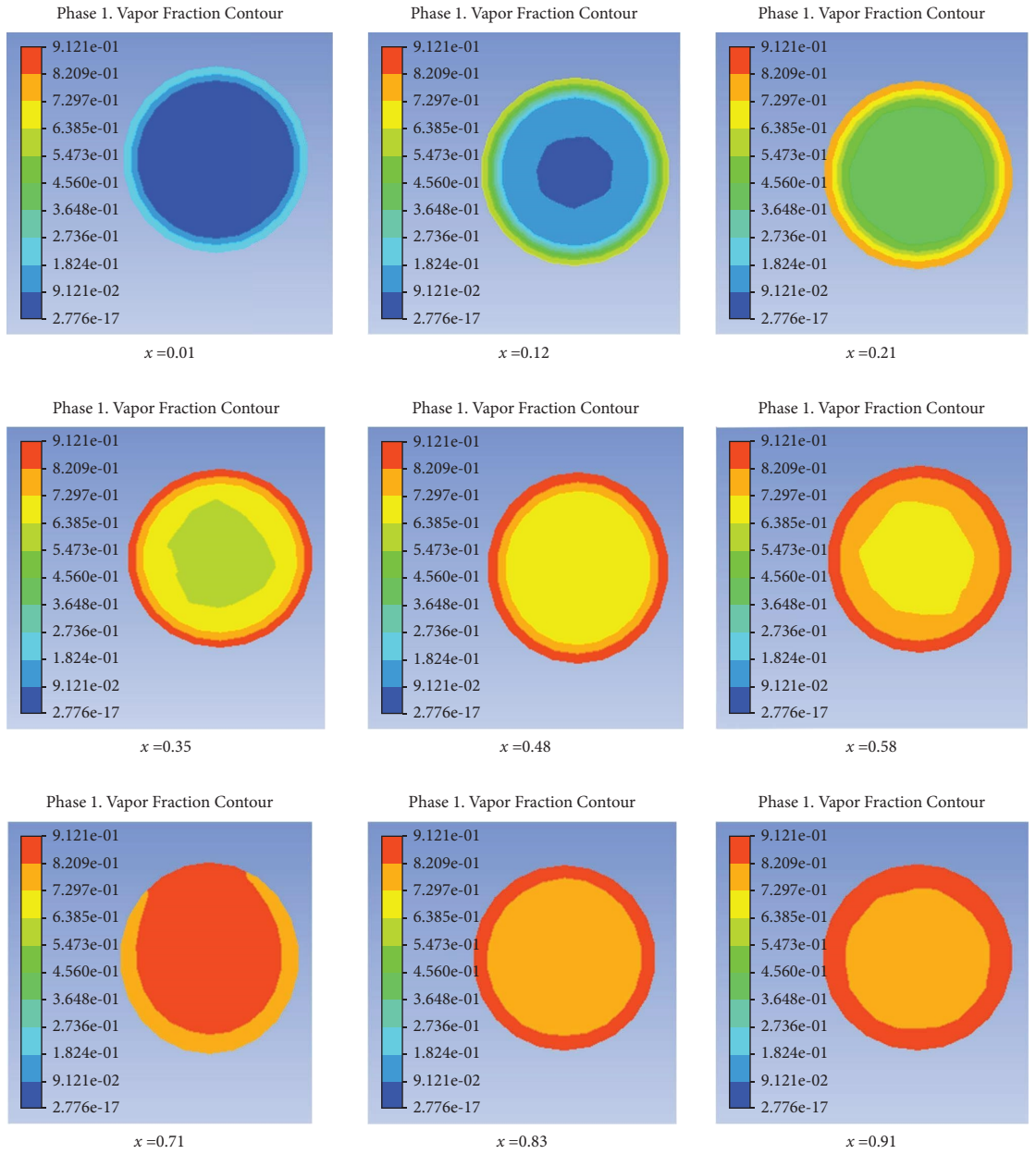

FIGURE 20: Flow formation for R1234yf-Al_2O_3 nanofluid and vapor quality within 0.01~0.91 occurred before the bend ($x = 0.01$ to 0.48), at the bend ($x = 0.58$ to 0.71), and after the bend ($x = 0.83$ to 0.91) at the mass flux of 160 kg/m^2·s and temperature of 350 K.

Figure 18(b), the velocity streamlines are parallel to the axis of the pipe and provide a visualization of the velocity distribution at any given moment in time.

Moreover, Figure 19 shows the flow formation of flow boiling evaporation of R1234yf in a U-bend tube, and the vapor forms and flows throughout the pipe. R1234yf at 350K temperature has 74% vapor faction. The evaporation starts from the adjacent liquid of the tube wall at 350 K temperature. Gradually, a vapor layer starts to form around the pipe wall. As the mixture of liquid and vapor moves along the pipe, the vapor layer also grows in thickness. At the bend section, fluid and vapor mixture passing through the bend is affected by various forces, such as the centrifugal force, density differences between phases, viscous forces, buoyancy forces, and gravitational forces. These forces cause secondary flows that alter the path of the fluid, resulting in a redistribution of the phases at the bend. As a result, the vapor fraction increasing rate accelerated. After the bend, the vapor form of R1234yf has shown quite a faster rate than before. It is shown that the flow formation of flow boiling evaporation occurred for the R1234yf refrigerant at the vapor fractions from 1% to 74% through the U-bend pipe.

In contrast, Figure 20 shows the flow formation of flow boiling evaporation of R1234yf-Al_2O_3 nanofluid in a U-bend tube. After mixing the nanoparticles with R1234yf, the vapor fraction increased from 74% to 91%. The evaporation starts from the adjacent liquid of the tube wall at 350 K

temperature. A vapor layer starts to form around the pipe wall. As the mixture of liquid and vapor moves along the pipe, the vapor layer is also growing in thickness. At the bend section, fluid and vapor mixture passing through the bend is affected by various forces, such as the centrifugal force, density differences between phases, viscous forces, buoyancy forces, and gravitational forces. These forces cause secondary flows that alter the path of the fluid, resulting in a redistribution of the phases at the bend. As a result, the vapor fraction increasing rate accelerated.

4. Conclusion

In this study, the VOF model was used to track the patterns at the gas-liquid interface, while the SST k-omega steady model was used to determine the gas-liquid flow. For the energy equation, the pressure-velocity coupling solution model with momentum being second-order upwind and vapor fraction being first-order upwind is applied. The investigation employed mass fluxes from 35 to 160 kg/m^2·s and vapor fractions between 0.01 and 0.91. The flow patterns, heat transfer coefficient, and pressure drop of R32 and R1234yf with Al_2O_3 nanoparticles in a U-bend tube with a curvature ratio of 2.50 were investigated using the CFD program Ansys Fluent®.

The following conclusions can be drawn:

(i) In flow boiling evaporation in a U-bend tube with a downward flow, the heat transfer coefficient is strongly influenced by the mass flux and vapor fraction. The heat transfer coefficients start to decline at the upper straight section of the pipe. The heat transfer coefficient is increased at the bend section and the flow separation facilitates convective heat transmission and changeover from stratified flow to annular flow. Heat transmission declines after the curve as the flow reverts to stratified flow. For constant mass fluxes, the heat transfer coefficients of R32 and R1234yf with Al_2O_3 nanoparticles are also increased for temperatures from 300 K to 400 K.

(ii) The frictional pressure drop of R32 and R1234yf with Al_2O_3 nanoparticles increases with mass fluxes and temperatures. When the mass flux rises, it also makes resistive pressure drop increase. This is due to an increase in the contact shear stress between the liquid and vapor phases, the two-phase fluid, and the tube wall.

(iii) Adding Al_2O_3 nanoparticles with R32 and R1234yf increases the heat transfer capability of these refrigerants and increases the frictional pressure drop. Mixing nanoparticles with refrigerant at different percentages certainly increased the heat transfer coefficient quite significantly, along with the vapor fraction, due to the higher heat conductivity of metal nanoparticles.

This work was performed with a fixed diameter and limited ranges of mass fluxes in a U-bend tube with the Al_2O_3 nanoparticle, and it can be further expanded on variable diameter, shapes of the tube, and various mass fluxes with different nanoparticles such as TiO_2, CuO, and SiO_2.

Data Availability

The datasets generated and analysed during the current study are not publicly available due to continuous studying but are available from the corresponding author on reasonable request.

Conflicts of Interest

The authors declare that they have no conflicts of interest.

Acknowledgments

The authors appreciate and acknowledge the Khulna University of Engineering & Technology for providing high-performance computing facilities and the University Grand Commission, Bangladesh, for the other support throughout this work.

References

[1] R. Hulse, R. Singh, and H. Pham, "Physical properties of HFO-1234yf," in *Proceedings of the 3rd Conference on Thermophysical Properties and Transfer Processes of Refrigerants*, pp. 23–26, IIFR, Boulder, US, 2009.

[2] R. Akasaka, "New fundamental equations of state with a common functional form for 2,3,3,3-tetrafluoropropene (R-1234yf) and trans-1,3,3,3-tetrafluoropropene (R-1234ze(E))," *International Journal of Thermophysics*, vol. 32, no. 6, pp. 1125–1147, 2011.

[3] X. Meng, G. Qiu, J. Wu, and I. M. Abdulagatov, "Viscosity measurements for 2,3,3,3-tetrafluoroprop-1-ene (R1234yf) and trans-1,3,3,3-tetrafluoropropene (R1234ze(E))," *The Journal of Chemical Thermodynamics*, vol. 63, pp. 24–30, 2013.

[4] E. J. K. Nilsson, O. J. Nielsen, M. S. Johnson, M. D. Hurley, and T. J. Wallington, "Atmospheric chemistry of cis-CF3CH=CHF: Kinetics of reactions with OH radicals and O3 and products of OH radical initiated oxidation," *Chemical Physics Letters*, vol. 473, no. 4–6, pp. 233–237, 2009.

[5] G. Myhre, D. Shindell, F. M. Bréon et al., "Anthropogenic and natural radiative forcing," in *Climate Change 2013: The Physical Science Basis*, vol. 9781107057, pp. 659–740, Cambridge University Press, Cambridge, UK, 2013.

[6] J. R. Juhasz, "Novel working fluid, HFO-1336mzz (E), for use in waste heat recovery application," in *Proceedings of the 12th IEA Heat Pump Conference*, pp. 1–10, HPC, Wilmington 19805, USA, 2017.

[7] D. Mondal, K. Kariya, A. R. Tuhin, N. Amakusa, and A. Miyara, "Viscosity measurement for trans-1,1,1,4,4,4-hexafluoro-2-butene (R1336mzz(E)) in liquid and vapor phases," *International Journal of Refrigeration*, vol. 133, pp. 267–275, 2022.

[8] D. Mondal, K. Kariya, A. R. Tuhin, K. Miyoshi, and A. Miyara, "Thermal conductivity measurement and correlation at saturation condition of HFO refrigerant trans-1,1,1,4,4,4-hexafluoro-2-butene (R1336mzz(E))," *International Journal of Refrigeration*, vol. 129, pp. 109–117, 2021.

[9] H. L. Wu, X. F. Peng, P. Ye, and Y. E. Gong, "Simulation of refrigerant flow boiling in serpentine tubes," *International*

Journal of Heat and Mass Transfer, vol. 50, no. 5–6, pp. 1186–1195, 2007.

[10] J. El Hajal, J. R. Thome, and A. Cavallini, "Condensation in horizontal tubes, part 1: two-phase flow pattern map," *International Journal of Heat and Mass Transfer*, vol. 46, no. 18, pp. 3349–3363, 2003.

[11] L. Cheng, G. Ribatski, L. Wojtan, and J. R. Thome, "Erratum to: "New flow boiling heat transfer model and flow pattern map for carbon dioxide evaporating inside horizontal tubes" [Heat Mass Transfer 49 (21–22) (2006) 4082–4094]," *International Journal of Heat and Mass Transfer*, vol. 50, no. 1–2, p. 391, 2007.

[12] A. Greco and G. P. Vanoli, "Flow-boiling of R22, R134a, R507, R404A and R410A inside a smooth horizontal tube," *International Journal of Refrigeration*, vol. 28, no. 6, pp. 872–880, 2005.

[13] S. Grauso, R. Mastrullo, A. W. Mauro, J. R. Thome, and G. P. Vanoli, "Flow pattern map, heat transfer and pressure drops during evaporation of R-1234ze(E) and R134a in a horizontal, circular smooth tube: experiments and assessment of predictive methods," *International Journal of Refrigeration*, vol. 36, no. 2, pp. 478–491, 2013.

[14] Z. Q. Yang, G. F. Chen, X. R. Zhuang et al., "A new flow pattern map for flow boiling of R1234ze(E) in a horizontal tube," *International Journal of Multiphase Flow*, vol. 98, pp. 24–35, 2018.

[15] M. Padilla, R. Revellin, and J. Bonjour, "Prediction and simulation of two-phase pressure drop in return bends," *International Journal of Refrigeration*, vol. 32, no. 7, pp. 1776–1783, 2009.

[16] K. D. Kerpel, S. D. Schampheleire, T. D. Keulenaer, and M. D. Paepe, "Effect of the bend geometry on the two-phase frictional pressure drop and flow behaviour in the vicinity of the bend," *Applied Thermal Engineering*, vol. 104, pp. 403–413, 2016.

[17] R. J. D. S. Lima and J. R. Thome, "Two-phase frictional pressure drops in U-bends and contiguous straight tubes for different refrigerants, orientations, tube, and bend diameters: Part 1. Experimental results (RP-1444)," *HVAC and amp;R Research*, vol. 18, no. 6, pp. 1047–1071, 2012.

[18] D. Lorenzini and Y. K. Joshi, "Computational fluid dynamics modeling of flow boiling in microchannels with nonuniform heat flux," *Journal of Heat Transfer*, vol. 140, no. 1, 2017.

[19] S. C. K. D. Schepper, G. J. Heynderickx, and G. B. Marin, "Modeling the evaporation of a hydrocarbon feedstock in the convection section of a steam cracker," *Computers & Chemical Engineering*, vol. 33, no. 1, pp. 122–132, 2009.

[20] S. M. A. N. R. Abadi, J. P. Meyer, and J. Dirker, "Effect of inclination angle on the condensation of R134a inside an inclined smooth tube," *Chemical Engineering Research and Design*, vol. 132, pp. 346–357, 2018.

[21] G. Lillo, R. Mastrullo, A. W. Mauro, and L. Viscito, "Flow boiling of R32 in a horizontal stainless steel tube with 6.00 mm ID. Experiments, assessment of correlations and comparison with refrigerant R410A," *International Journal of Refrigeration*, vol. 97, pp. 143–156, 2019.

[22] D. Lorenzini, Y. Joshi, and G. W. Woodruff, "Numerical modeling and experimental validation of two-phase microfluidic cooling in silicon devices for vertical integration of microelectronics," *International Journal of Heat and Mass Transfer*, vol. 138, pp. 194–207, 2019.

[23] J. D. Li, "CFD simulation of water vapour condensation in the presence of non-condensable gas in vertical cylindrical condensers," *International Journal of Heat and Mass Transfer*, vol. 57, no. 2, pp. 708–721, 2013.

[24] C. Aprea, A. Greco, A. Maiorino, C. Masselli, and A. Metallo, "HFO1234ze as drop-in replacement for R134a in domestic refrigerators: an environmental impact analysis," *Energy Procedia*, vol. 101, pp. 964–971, 2016.

[25] A. Maiorino, R. Llopis, M. G. D. Duca, and C. Aprea, "Environmental impact assessment of R-152a as a drop-in replacement of R-134a in a domestic refrigerator," *International Journal of Refrigeration*, vol. 117, pp. 132–139, 2020.

[26] J. Soni, V. Gupta, Y. Joshi et al., "Investigative comparison of R134a, R290, R600a and R152a refrigerants in conventional vapor compression refrigeration system," *Materials Today: Proceedings*, 2023.

[27] K. Mallikarjuna, K. HemachnadraReddy, and M. NagaRaju, "Experimental investigation on nano refrigeration using TiO_2, CuO, and Al_2O_3 as refrigerants," *Materials Today: Proceedings*, 2023.

[28] B. S. Bibin, P. Amartya, K. Govil, and G. Edison, "Performance of refrigeration system using Al_2O_3, CuO, and TiO_2 nano-enhanced refrigerants: a review," *Materials Today: Proceedings*, 2023.

[29] A. S. Majgaonkar, "Use of nanoparticles in refrigeration systems: a literature review paper," in *Proceedings of the International Refrigeration and Air Conditioning Conferences*, pp. 1–10, Purdue University, WL, USA, July 2016.

[30] H. Peng, G. Ding, and H. Hu, "Influences of refrigerant-based nanofluid composition and heating condition on the migration of nanoparticles during pool boiling. Part I: experimental measurement," *International Journal of Refrigeration*, vol. 34, no. 8, pp. 1823–1832, 2011.

[31] G. Ding, H. Peng, W. Jiang, and Y. Gao, "The migration characteristics of nanoparticles in the pool boiling process of nanorefrigerant and nanorefrigerant-oil mixture," *International Journal of Refrigeration*, vol. 32, no. 1, pp. 114–123, 2009.

[32] D. C. Hernández, C. Nieto-Londoño, and Z. Zapata-Benabithe, "Analysis of working nanofluids for a refrigeration system," *Dyna*, vol. 83, no. 196, pp. 176–183, 2016.

[33] D. S. Kumar and R. Elansezhian, "Experimental study on Al_2O_3-R134a nano refrigerant in refrigeration system," *International Journal of Modern Engineering Research*, vol. 2, no. 5, pp. 3927–3929, 2012.

[34] M. V. Royal, M. Ahamed, R. Kumar, and Y. H. Krishna, "Experimental study on Al_2O_3-R134a nano refrigerant in refrigeratuin system," *Journal of Emerging Technologies and Innovative Research*, vol. 6, no. 5, pp. 161–166, 2019.

[35] J. Vamshi, K. M. Anand, A. Sharma et al., "A review on the utilization of nanoparticles in the refrigeration system as nano-refrigerant and nano-lubricant," *Materials Today: Proceedings*, vol. 50, pp. 782–788, 2022.

[36] T. Jatau and T. Bello-Ochende, "Heat transfer and flow pattern map development of R134a in a U-bend tube for flow boiling evaporation," *International Communications in Heat and Mass Transfer*, vol. 128, Article ID 105629, 2021.

[37] Refrigerator, "Mechanical engineering," 2016, http://www.mecha-engineeringbd.com/2016/07/refrigerator.html.

[38] U. Coil & Air, "DX evaporator coils," 2021, https://usacoil.com/dx-evaporator-coils/.

[39] R. J. D. S. Lima and J. R. Thome, "Two-phase flow patterns in U-bends and their contiguous straight tubes for different orientations, tube and bend diameters," *International Journal of Refrigeration*, vol. 35, no. 5, pp. 1439–1454, 2012.

[40] H. I. Mohammed, D. Giddings, and G. S. Walker, "CFD multiphase modelling of the acetone condensation and evaporation process in a horizontal circular tube," *International Journal of Heat and Mass Transfer*, vol. 134, pp. 1159–1170, 2019.

[41] M. H. Oudah, M. K. Mejbel, and M. K. Allawi, "R134a flow boiling heat transfer (FBHT) characteristics in a refrigeration system," *Journal of Mechanical Engineering Research and Developments*, vol. 44, no. 4, pp. 69–83, 2021.

[42] R. Zhuan and W. Wang, "Flow pattern of boiling in microchannel by numerical simulation," *International Journal of Heat and Mass Transfer*, vol. 55, no. 5–6, pp. 1741–1753, 2011.

[43] A. Kamyar, R. Saidur, and M. Hasanuzzaman, "Application of computational fluid dynamics (CFD) for nanofluids," *International Journal of Heat and Mass Transfer*, vol. 55, no. 15–16, pp. 4104–4115, 2012.

[44] M. Richter, M. O. McLinden, and E. W. Lemmon, "Thermodynamic properties of 2,3,3,3-Tetrafluoroprop-1-ene (R1234yf): vapor pressure and P-ρ-T measurements and an equation of state," *Journal of Chemical and Engineering Data*, vol. 56, no. 7, pp. 3254–3264, 2011.

[45] E. W. Lemmon, I. H. Bell, M. L. Huber, and M. O. McLinden, *NIST Standard Reference Database 23: Reference Fluid Thermodynamic Properties-REFPROP (DLL Version 10.0a)*, NIST, USA, 2018.

[46] M. L. Huber, "Models for viscosity, thermal conductivity, and surface tension of selected pure fluids as implemented in REFPROP v10.0," 2018, https://nvlpubs.nist.gov/nistpubs/ir/2018/NIST.IR.8209.pdf.

[47] C. C. Wang, I. Youn Chen, Y. W. Yang, and R. Hu, "Influence of horizontal return bend on the two-phase flow pattern in small diameter tubes," *Experimental Thermal and Fluid Science*, vol. 28, no. 2–3, pp. 145–152, 2004.

[48] P. O. Ayegba, L. C. Edomwonyi-Otu, A. Abubakar, and N. Yusuf, "Flow pattern and pressure drop for oil–water flows in and around 180° bends," *SN Applied Sciences*, vol. 3, no. 1, pp. 10–13, 2021.